



The transcriptional coactivator CBP/p300 is an evolutionarily conserved node that promotes longevity in response to mitochondrial stress

Terytty Yang Li¹, Maroun Bou Sleiman^{1,2}, Hao Li¹, Arwen W. Gao¹, Adrienne Mottis¹, Alexis Maximilien Bachmann¹, Gaby El Alam¹, Xiaoxu Li¹, Ludger J. E. Goeminne¹, Kristina Schoonjans^{1,2} and Johan Auwerx¹✉

Organisms respond to mitochondrial stress by activating multiple defense pathways, including the mitochondrial unfolded protein response (UPR^{mt}). However, how UPR^{mt} regulators are orchestrated to transcriptionally activate stress responses remains largely unknown. Here, we identify CREB-binding protein-1 (CBP-1), the worm ortholog of the mammalian acetyltransferases CBP/p300, as an essential regulator of the UPR^{mt}, as well as the mitochondrial stress-induced immune response, with involvement also in the reduction of amyloid- β aggregation and lifespan extension in *Caenorhabditis elegans*. Mechanistically, CBP-1 acts downstream of the histone demethylases JMJD-1.2 and JMJD-3.1 and upstream of UPR^{mt} transcription factors, including ATFS-1, to systematically induce a broad spectrum of UPR^{mt} genes and execute multiple beneficial functions. In mouse and human populations, transcript levels of *CBP/p300* positively correlate with UPR^{mt} transcripts and longevity. Furthermore, *CBP/p300* inhibition disrupts the UPR^{mt} in mammalian cells, while forced expression of *p300* is sufficient to activate it. These results highlight an evolutionarily conserved mechanism that determines the mitochondrial stress response and promotes health and longevity through *CBP/p300*.

Mitochondria not only contribute to the harvesting of energy, but also serve as key signaling hubs connecting numerous metabolic processes to essential cellular and organismal functions^{1–3}. It is therefore not surprising that the dysfunction of mitochondria is tightly associated with aging, as well as diverse human age-related diseases, including those affecting metabolic, cardiovascular and neuromuscular systems, as well as cancer^{2,4–7}. Moreover, mitochondria function as platforms to regulate programmed cell death and innate immune responses^{1,8,9}. Multiple mitochondrial stress response (MSR) pathways have evolved to adapt mitochondrial function to the ever-changing cellular milieu and to a variety of extracellular cues^{10,11}. However, aberrant activation of these MSR pathways may also be maladaptive and contribute to disease and aging², underscoring the importance of the tight control of these regulatory circuits.

The mitochondrial unfolded protein response (UPR^{mt}), one of these MSR pathways, is triggered by mitochondrial-to-nuclear communication, leading to an adaptive transcriptional response that promotes repair and recovery of the cell or organism from transient mitochondrial dysfunction^{10–13}. It recently emerged that activation of the UPR^{mt} provides resistance to pathogen infections (for example, *Pseudomonas aeruginosa*) in *Caenorhabditis elegans*, and animals that failed to activate UPR^{mt} during *P. aeruginosa* infection died earlier, suggesting that the UPR^{mt} is a bona fide component of the innate immune response^{14,15}. In mammalian cells, mitochondrial perturbations also lead to cellular stress responses closely associated with innate immunity^{9,16}; for example, herpesvirus infections induce a mitochondrial DNA stress response, which enhances antiviral signaling and type I interferon responses and thereby confers viral resistance¹⁷.

The regulation of the UPR^{mt} is complex and pleiotropic, and includes control at the level of transcription and chromatin organization. At the transcriptional level, the activating transcription factor associated with stress-1 (ATFS-1) in *C. elegans*¹⁸, and its functional orthologs activating transcription factor 4 (ATF4), ATF5 and C/EBP homologous protein (CHOP) in mammals^{19–21}, seem to be key regulators of the UPR^{mt}. Two recent studies suggest that an overlapping with the *m*-AAA protease 1 (OMA1)–DAP3 binding cell death enhancer 1 (DELE1)–heme-regulated eIF2 α kinase (HRI) signaling pathway relays the mitochondrial stress from mitochondria to the cytosol in mammals^{22,23}. On the epigenetic level, the histone methyltransferase MET-2/nuclear co-factor LIN-65 complex and two histone demethylases, jumonji domain-containing protein-1.2 (JMJD-1.2)/PHD finger protein 8 (PHF8) and JMJD-3.1/lysine demethylase 6B (KDM6B), regulate the UPR^{mt} and mitochondrial stress-induced longevity in both *C. elegans* and mammals^{24,25}, whereas in yeast the histone demethylase Rph1p is the key modulator²⁶. However, how these different layers of UPR^{mt} regulation is systematically coordinated to induce the expression of various UPR^{mt} genes and execute different biological functions is still poorly understood.

Here, we demonstrate that CREB-binding protein-1 (CBP-1) acts as an essential link to translate the mitochondrial stress signal from the demethylases JMJD-1.2 and JMJD-3.1 to the UPR^{mt} transcription factors (for example, ATFS-1) into the coordinated transcriptional induction of a wide panel of UPR^{mt} genes in *C. elegans*. Importantly, the beneficial effects induced by mitochondrial perturbations, such as resistance to pathogen infection, improved proteostasis against amyloid- β (A β) aggregation, and lifespan extension,

¹Laboratory of Integrative Systems Physiology, Interfaculty Institute of Bioengineering, École Polytechnique Fédérale de Lausanne, Lausanne, Switzerland.

²Laboratory of Metabolic Signaling, Interfaculty Institute of Bioengineering, École Polytechnique Fédérale de Lausanne, Lausanne, Switzerland.

✉e-mail: admin.auwerx@epfl.ch

are almost completely blocked by *cbp-1* silencing. Moreover, systematic correlation analysis in mouse and human populations, as well as genetic and pharmacological loss-of-function (LOF) studies in mammalian cells, strongly suggest that the function of CBP/p300 in the regulation of the UPR^{mt}, health and lifespan is also conserved in mammals. Collectively, these results highlighted that CBP/p300 is an evolutionarily conserved node for mitochondrial stress signaling that defends mitochondrial function and promotes health and longevity.

Results

CBP-1 controls UPR^{mt} activation in *C. elegans*. We used a UPR^{mt} activation model by knocking down *cytochrome c oxidase-1* (*cco-1*) in the UPR^{mt} reporter *hsp-6p::gfp* strain^{27,28} and performed an RNA interference (RNAi) screen by feeding RNAi targeting all putative lysine acetyltransferases (KATs) in *C. elegans* (Extended Data Fig. 1a)^{29–32}. Only RNAi of *cbp-1* (*R10E11.1*)³³, the ortholog of human CBP/p300 (refs. 34–37), attenuated UPR^{mt} activation to a similar extent as the silencing of the key UPR^{mt} transcription factor *atfs-1* (Fig. 1a and Extended Data Fig. 1b)¹⁸. The effect of *cbp-1* RNAi on UPR^{mt} activation induced by RNAi-mediated LOF of *cco-1* and mitochondrial ribosomal protein S5 (*mrps-5*)¹³ was furthermore dose dependent (Fig. 1b and Extended Data Fig. 1c,d). Moreover, another RNAi clone (*cbp-1*_RNAi_2), targeting a different region of the *cbp-1* messenger RNA (mRNA) compared with the one used in the RNAi screening (*cbp-1*_RNAi_1), also impaired UPR^{mt} activation (Extended Data Fig. 1e,f).

As an alternative approach to inhibit CBP-1 activity, we used two mechanistically different small-molecule inhibitors: a highly specific CBP/p300 catalytic inhibitor, A-485 (ref. 38); and a CBP/p300 bromodomain inhibitor, PF-CBP1 (Extended Data Fig. 1e)³⁹. Both inhibitors suppressed UPR^{mt} activation induced by *cco-1* or *mrps-5* RNAi, with A-485 having effects at a lower concentration (10 μM) compared with PF-CBP1 (80 μM) (Fig. 1c and Extended Data Fig. 1g). Likewise, genetic or pharmacological inductions of the UPR^{mt} by LOF of *spg-7*, *timmm-23*, *tomm-40*, *cts-1* and *dlst-1*, or by administering antimycin A and doxycycline (Dox)^{13,14,40}, were abolished by *cbp-1* RNAi (Fig. 1d,e). Of note, UPR^{mt} activation was not affected by RNAi that specifically targeted the two probable pseudogenes of *cbp-1*, *cbp-2* and *cbp-3* (Extended Data Fig. 1h,i), both of which lack most of the functional domains compared with CBP-1, including the histone acetyltransferase domain (Extended Data Fig. 1j)³³. *cbp-1* RNAi also attenuates activation of the endoplasmic reticulum UPR, but not the cytosolic UPR/heat shock response in *C. elegans*, suggesting some activity in cross-modal stress response pathways (Extended Data Fig. 1k–n).

To determine the footprints of CBP-1 on the regulation of the UPR^{mt}, we performed RNA sequencing (RNA-seq) on total RNA isolated from *hsp-6p::gfp* worms fed with *cco-1* or *mrps-5* RNAi, in combination with *cbp-1* or *atfs-1* RNAi (Extended Data Fig. 2a and Supplementary Table 1). The majority of transcripts induced by *mrps-5* RNAi were also induced by *cco-1* RNAi, but not the other way around (Extended Data Fig. 2b), which might have been due to the superior knockdown efficiency of *cco-1* compared with that of *mrps-5* (Extended Data Fig. 2c). We thus focused on the genes affected by *cco-1* RNAi. A total of 1,241 transcripts were significantly upregulated after *cco-1* RNAi (\log_2 [fold change] > 0.5; adjusted $P < 0.05$; defined here as UPR^{mt} genes), among which 506 (40.8%) were CBP-1 dependent and 404 (32.6%) required ATFS-1 (Fig. 1f,g). The number of ATFS-1-dependent transcripts was similar to that found in a previous study¹⁸. Up to 259 genes induced by *cco-1* RNAi were dependent on both CBP-1 and ATFS-1 (Fig. 1g). Gene Ontology analysis revealed that a large number of mitochondrion-, transmembrane transport- and metabolic process-related genes, including *hsp-6*, *timmm-23* and *gpd-2*, required both CBP-1 and ATFS-1 for induction (Fig. 1h,j and Extended Data Fig. 2d). In addition,

many innate immune genes, such as the C-type lectin, *clec-65*, were also included in this gene set (Fig. 1f,h,j), supporting a role of UPR^{mt} in regulating the immune response^{14,15}.

Among the 506 UPR^{mt} transcripts regulated by CBP-1, 247 (48.8%) were only dependent on CBP-1, but not ATFS-1 (Fig. 1g), and were enriched for innate immune response (for example, *clec-70*), proteolysis (for example, *asp-10*) and metabolic processes (for example, *gdh-1*) (Fig. 1i,j and Extended Data Fig. 2e). Consistent with the role of ceramide biosynthesis in mitochondrial surveillance^{14,41}, *sptl-2*, which encodes a serine palmitoyltransferase, was robustly induced after *cco-1* or *mrps-5* knockdown in a CBP-1- but not ATFS-1-dependent fashion (Extended Data Fig. 2f). Moreover, other UPR^{mt} inducers, including LOF of *spg-7*, *timmm-23*, *tomm-40*, *cts-1* and *dlst-1*, not only led to the induction of CBP-1 and ATFS-1 commonly dependent UPR^{mt} transcripts (for example, *hsp-6*), but also upregulated UPR^{mt} transcripts that were only dependent on CBP-1 but not ATFS-1 (for example, *clec-70*) (Extended Data Fig. 2g).

In response to *cco-1* RNAi, 1,354 transcripts were significantly downregulated (\log_2 [fold change] < -0.5; adjusted $P < 0.05$) (Extended Data Fig. 2h and Supplementary Table 2); among these transcripts, 709 (52.4%) were also downregulated, and 190 (14.0%) were conversely upregulated, after *cbp-1* RNAi (Extended Data Fig. 2h). Interestingly, both gene clusters were enriched for metabolic process, oxidation-reduction process and carbohydrate metabolic process (Extended Data Fig. 2i,j), indicating a global rewiring of metabolism during mitochondrial stress^{19,21,42,43} and highlighting the vital role of *cbp-1* in this reprogramming. Finally, most transcripts downregulated after *mrps-5* RNAi were also downregulated during *cco-1* silencing (Extended Data Fig. 2k). Taken together, these data suggest that CBP-1 controls the induction of a broad spectrum of UPR^{mt} genes upon various mitochondrial stresses in *C. elegans*.

Mitochondrial stress increases CBP-1-mediated histone acetylation at the loci of UPR^{mt} genes. Next, we sought to explore the molecular mechanism by which CBP-1 regulates UPR^{mt} activation. CBP/p300, the mammalian homologues of CBP-1, are acetyltransferases involved in histone acetylation^{36,37}. In worms fed with *cco-1* and *mrps-5* RNAi, the global histone 3 acetylation at K18 (H3K18Ac) was increased by 60 and 40%, and H3K27Ac was increased by 90 and 20%, respectively, compared with worms fed with control RNAi (Fig. 2a). This increase was remarkably attenuated by *cbp-1* RNAi. Similar results were also found for H4K5Ac (Extended Data Fig. 3a), while H3K4Ac and H3K9Ac levels were not affected by *cbp-1* knockdown. RNAi for *atfs-1* did not alter the levels of any of the histone modifications examined (Fig. 2a and Extended Data Fig. 3a). Moreover, the CBP/p300 catalytic inhibitor, A-485, also impaired H3K18Ac and H3K27Ac, but not H3K9Ac, under *cco-1* knockdown (Fig. 2b). Additionally, other UPR^{mt} inducers, including LOF of *spg-7*, *timmm-23*, *tomm-40*, *cts-1* and *dlst-1*, increased H3K18Ac by 90% to 170%, and H3K27Ac by 30% to 150% (Fig. 2c).

It has been known that acetylation of H3K18 and H3K27, which transforms the condensed chromatin into a more relaxed structure, is generally linked to active transcription^{29,30,32,44}. To examine whether CBP-1-mediated histone acetylation contributes to the transcriptional activation of UPR^{mt} genes, we performed chromatin immunoprecipitation sequencing (ChIP-seq) with antibodies against H3K18Ac and H3K27Ac in worms fed with control or *cco-1* RNAi. Among the 506 UPR^{mt} genes regulated by CBP-1 (Fig. 1g), 203 had enriched H3K18Ac or H3K27Ac peaks in the genome (Fig. 2d). Importantly, 66.0% (134/203) of these UPR^{mt} genes (for example, *hsp-6*, *timmm-23*, *hsp-60* and *gpd-2*) demonstrated significantly increased levels of H3K18Ac or H3K27Ac (110 genes for H3K18Ac ($P < 1.9 \times 10^{-10}$; Fisher's exact test) and 76 genes for H3K27Ac ($P < 1.5 \times 10^{-12}$; Fisher's exact test)) after *cco-1* RNAi (false discovery rate (FDR) < 0.05) (Fig. 2d–g, Extended Data Fig. 3b and Supplementary Table 3). In contrast, no differences in

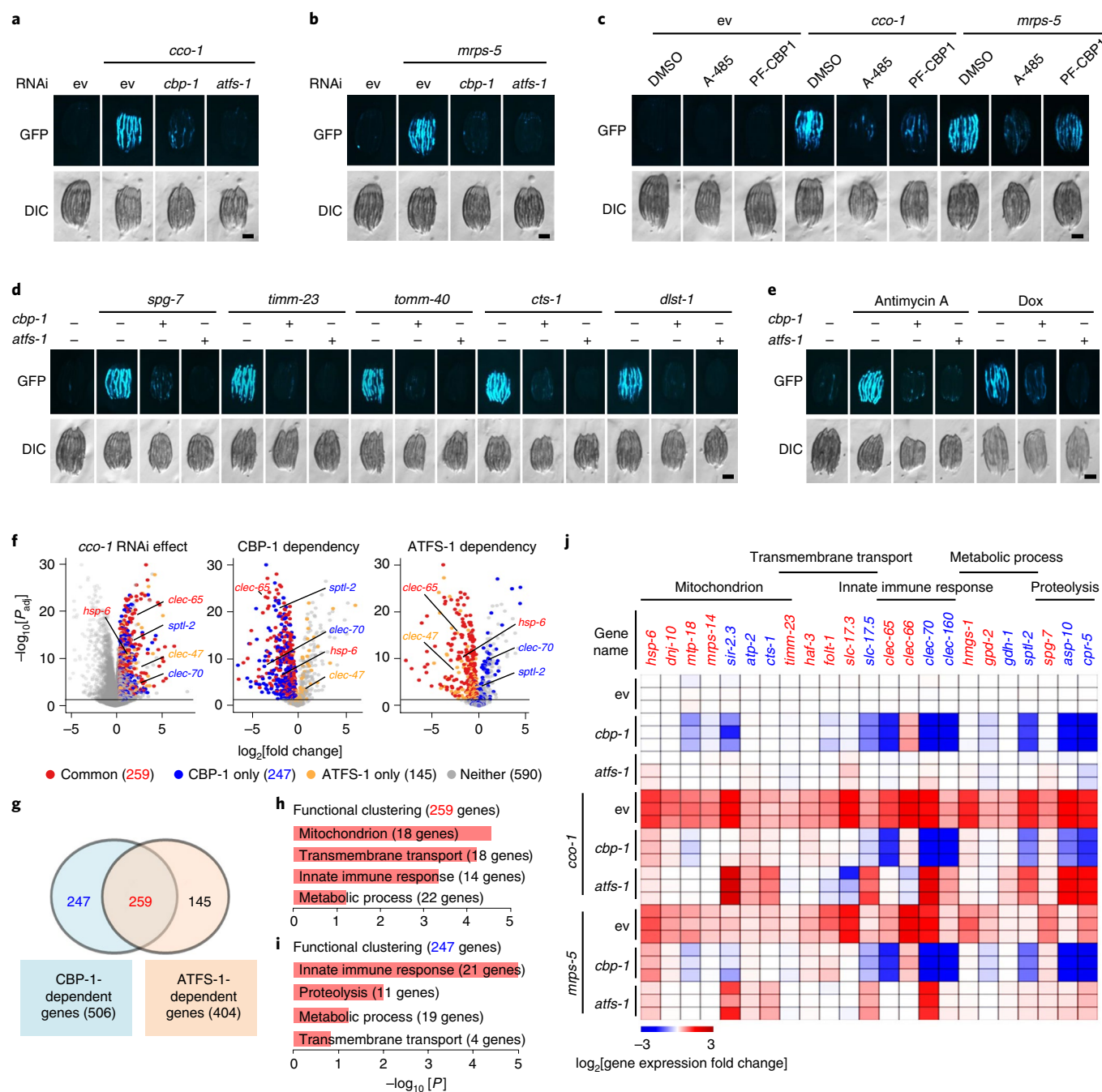


Fig. 1 | CBP-1 controls activation of the UPR^{mt} in C. elegans. **a, b**, *cbp-1* RNAi attenuates UPR^{mt} activation induced by *cco-1* (a) or *mrps-5* (b) knockdown in *hsp-6p::gfp* worms. For RNAi treatment, RNAi targeting *cco-1* or *mrps-5* occupies 40%, *cbp-1* RNAi occupies 25% and *atfs-1* RNAi occupies 60%. Control RNAi (empty vector (ev)) was used to supply to a final 100% of RNAi for all conditions. DIC, differential interference contrast. **c**, The CBP/p300 small-molecule inhibitors A-485 and PF-CBP1 attenuate UPR^{mt} activation in worms. *hsp-6p::gfp* worms were fed with control or UPR^{mt}-inducing *cco-1* (40%) RNAi, in combination with A-485 (10 μM) or PF-CBP1 (80 μM) treatment. **d, e**, *cbp-1* RNAi abolishes UPR^{mt} activation induced by *spg-7*, *timm-23*, *tomm-40*, *cts-1* or *dlst-1* RNAi (d), and by antimycin A (2.5 μM) or Dox (30 μg ml⁻¹) (e), in *hsp-6p::gfp* worms. The *atfs-1* RNAi was used as a positive control. RNAi targeting *tomm-40*, *cts-1* or *dlst-1* occupies 40%, *cbp-1* RNAi occupies 25% and *atfs-1* RNAi occupies 60%. **f**, Volcano plots showing the effects on gene expression of *cco-1* RNAi compared with the control RNAi (ev) (left), and of *cbp-1* (middle) or *atfs-1* (right) knockdown in a *cco-1* RNAi background. Genes dependent on both CBP-1 and ATFS-1 for induction after *cco-1* RNAi are highlighted in red (common). Genes dependent on CBP-1, but not ATFS-1, for induction are in blue (CBP-1 only). Genes dependent on ATFS-1, but not CBP-1, for induction are highlighted in orange (ATFS-1 only). *P*_{adj}, adjusted *P* value. **g**, Venn diagram of CBP-1-dependent UPR^{mt} genes that are in common with ATFS-1-dependent UPR^{mt} genes in response to *cco-1* RNAi, according to the RNA-seq data. **h, i**, Functional clustering of the 259 (h) and 247 (i) UPR^{mt} genes as indicated in g. **j**, Heatmap of the representative UPR^{mt} genes dependent on CBP-1 for induction during *cco-1* knockdown. The color coding represents gene expression differences in log₂[fold change] relative to the control RNAi (ev) condition. Genes dependent on both CBP-1 and ATFS-1 are highlighted in red. Genes dependent on CBP-1, but not ATFS-1, are highlighted in blue. Scale bars (a–e), 0.3 mm.

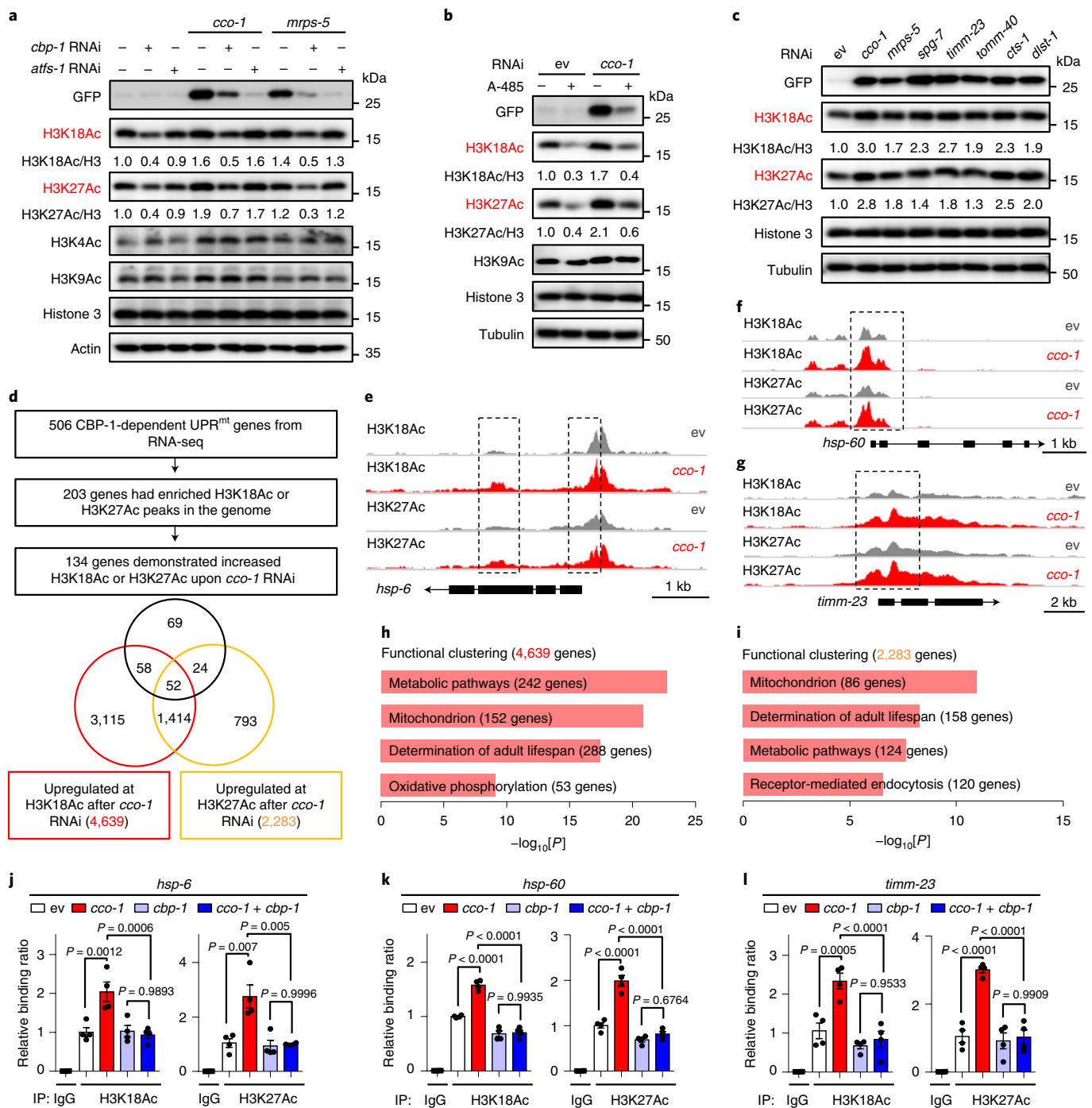


Fig. 2 | Mitochondrial stress increases CBP-1-dependent histone acetylation at the loci of a large set of UPR^{mt} genes. **a**, H3K18 and H3K27 acetylation increases in a CBP-1-dependent manner during UPR^{mt} activation induced by *cco-1* or *mrps-5* RNAi. Western blots of *hsp-6p::gfp* worms fed with control, *cbp-1*, *atfs-1*, *cco-1* or *mrps-5* RNAi are shown. RNAi targeting *cbp-1* occupies 25% and *atfs-1*, *cco-1* or *mrps-5* occupies 50%. Control RNAi was used to supply to a final 100% of RNAi for all conditions. **b**, The increase of H3K18Ac and H3K27Ac upon *cco-1* RNAi is strongly blocked by chemical inhibition of CBP/p300 with A-485. Western blots of *hsp-6p::gfp* worms fed with control or *cco-1* (50%) RNAi are shown, in combination with DMSO or A-485 (10 μ M) treatment. **c**, Western blots of *hsp-6p::gfp* worms showing increased H3K18Ac and H3K27Ac during UPR^{mt} activation induced by RNAi targeting different mitochondrial genes, as indicated. **d**, Summary of the H3K27Ac and H3K18Ac ChIP-seq results in worms fed with control or *cco-1* RNAi. **e-g**, Treatment of *cco-1* RNAi increases H3K18Ac and H3K27Ac at the genomic loci of representative UPR^{mt} genes including *hsp-6*, *hsp-60* and *timm-23*. Genome tracks show the ChIP-seq analysis for H3K27Ac and H3K18Ac over the genomic loci of *hsp-6* (**e**), *hsp-60* (**f**) and *timm-23* (**g**) in worms fed with control (ev) or *cco-1* RNAi. The two tracks are shown with the same total count range between basal and mitochondrial stress conditions for each gene. **h,i**, Functional clustering of the 4,639 (**h**) and 2,283 (**i**) genes as indicated in **d**. **j-l**, *cco-1* RNAi-induced increase of H3K18Ac and H3K27Ac at the loci of representative UPR^{mt} genes is completely blocked by *cbp-1* RNAi. The results of ChIP-qPCR analysis of *hsp-6* (**j**), *hsp-60* (**k**) and *timm-23* (**l**) in worms fed with RNAi targeting *cco-1* and/or *cbp-1* ($n = 4$ biologically independent samples) are shown. RNAi targeting *cco-1* occupies 50% and *cbp-1* occupies 25%. ChIP was performed using antibodies to H3K18Ac or H3K27Ac. Error bars denote s.e.m. Statistical significance was determined by ANOVA followed by Tukey's post-hoc test. IgG, immunoglobulin G; IP, immunoprecipitation.

H3K18Ac or H3K27Ac marks were observed for the endoplasmic reticulum UPR markers *hsp-3* and *hsp-4*, or for the cytosolic UPR/heat shock response marker *hsp-16.2*, upon *cco-1* RNAi treatment (Extended Data Fig. 3c–e). By analyzing the distribution of the 265 increased H3K18Ac/H3K27Ac peaks on the 134 UPR^{mt} genes, we found that 54.0% (143/265) of them were located in promoter regions, 40.0% (106/265) were in coding regions and 6.0% (16/265) were downstream of the coding region (Extended Data Fig. 3f and Supplementary Table 3). Indeed, for some genes (for example, *hsp-60*), acetylation peaks are restricted to the promoter (Fig. 2f), whereas for other genes (for example, *hsp-6* and *timmm-23*), acetylation marks exist in both promoter and coding regions (Fig. 2e,g). It is also noteworthy that both gene sets upregulated for the acetylation marks in response to *cco-1* RNAi (4,639 genes for H3K18Ac and 2,283 genes for H3K27Ac) were highly enriched for Gene Ontology terms including metabolic pathways, mitochondrion, and determination of adult lifespan (Fig. 2h,i and Supplementary Table 3), supporting a critical role of these epigenetic adaptations in the control of mitochondrial metabolism and lifespan upon mitochondrial stress. Using ChIP coupled with quantitative PCR (ChIP-qPCR), we detected that the increased enrichment of H3K18Ac and H3K27Ac at the loci of UPR^{mt} genes (for example, *hsp-6*, *hsp-60* and *timmm-23*) in response to *cco-1* knockdown was completely blocked by *cbp-1* RNAi (Fig. 2j–l). These results indicate that increased CBP-1-dependent histone acetylation upon mitochondrial stress is closely associated with the transcriptional activation of a large set of UPR^{mt} genes.

CBP-1 acts downstream of JMJD-3.1/JMJD-1.2 and upstream of ATFS-1. Two histone demethylases, JMJD-3.1 and JMJD-1.2, have been reported to remove the repressive H3K27me3 mark from the promoter/coding regions of UPR^{mt} genes, poisoning them for transcription, and overexpression of *jmjd-3.1* in worms is sufficient to activate the UPR^{mt} (ref. 25). RNAi for *cbp-1* abolished activation of the UPR^{mt} in two independently generated *jmjd-3.1*-overexpressing strains (Fig. 3a). Moreover, increased levels of H3K18Ac and H3K27Ac, but not H3K9Ac, were detected in *jmjd-3.1*-overexpressing worms, and this was attenuated by *cbp-1* RNAi (Fig. 3b). In addition, 177 (35.0%) of the 506 CBP-1-dependent UPR^{mt} transcripts were also induced in *jmjd-3.1*-overexpressing worms (GSE78990) (Fig. 3c,d and Supplementary Table 4), and 129 (72.9%) of these 177 UPR^{mt} transcripts were also upregulated upon *jmjd-1.2* overexpression (Supplementary Table 4), underscoring a positive role of CBP-1 in the regulation of the MSR. Notably, *cbp-1* stood out as the most upregulated transcript among all of the 13 putative KATs in *jmjd-3.1*-overexpressing worms (Fig. 3e).

To further explore how CBP-1 affects the transcriptional activation of UPR^{mt} genes, we took advantage of the *atfs-1(et18)* mutant⁴⁵, which carries a mutation in the mitochondrial targeting sequence of the transcription factor ATFS-1, leading to its nuclear accumulation and constitutive activation of the UPR^{mt}. Silencing of *cbp-1* blocked UPR^{mt} activation in the *atfs-1(et18)* mutant (Fig. 3f,g). Moreover, ATFS-1 failed to bind to the promoters of UPR^{mt} genes (for example, *hsp-6* and *hsp-60*) in *cbp-1* RNAi-fed *atfs-1p::atfs-1::flag* worms, even during mitochondrial stress induced by *cco-1* RNAi (Fig. 3h). Collectively, these data indicate that *jmjd-3.1*-overexpression-mediated UPR^{mt} activation requires CBP-1, and CBP-1-dependent histone acetylation acts downstream of JMJD-3.1 and JMJD-1.2 at the same time as upstream of ATFS-1, leading to transcriptional induction of UPR^{mt} genes.

Beneficial effects of UPR^{mt} require CBP-1. We then explored the physiological consequences of CBP-1 on MSR regulation. In line with the fact that mild mitochondrial stress protects against infection by pathogens, such as *P. aeruginosa*^{14,15}, *cco-1* or *mrrps-5* knockdown increased the survival rate of worms exposed to *P. aeruginosa*, an effect that was completely abolished by *cbp-1* knockdown (Fig. 4a,b).

To further examine the vital role of CBP-1 in mitochondrial surveillance, we raised wild-type worms (N2) and mitochondrial respiration mutants with disruptions in one of the mitochondrial electron transport chain components, *isp-1(qm150)* and *clk-1(qm30)*^{46,47}, on control or *cbp-1* RNAi. Compared with *C. elegans* fed with control RNAi, *cbp-1* RNAi even at 10% led to severe synthetic growth defects of the *isp-1(qm150)* and *clk-1(qm30)* mutants, whereas the development of wild-type worms was only slightly delayed (Fig. 4c). Similar effects were also observed in A-485-treated worms (Fig. 4c), indicating that mitochondrial mutants strongly rely on CBP-1 activity to maintain growth.

We then questioned whether *cbp-1* is required for mitochondrial stress-induced lifespan extension in *C. elegans*^{13,48}. RNAi for *cbp-1* at 20%, which was enough to suppress the UPR^{mt} activation induced by *cco-1* knockdown (Extended Data Fig. 1c), completely blocked the lifespan extension induced by *cco-1* RNAi (Fig. 4d). Likewise, *cbp-1* RNAi at 10% fully abolished *mrrps-5* knockdown-induced lifespan extension (Fig. 4e), in line with its capacity to block *mrrps-5* RNAi-induced UPR^{mt} activation (Extended Data Fig. 1d). Meanwhile, consistent with the results of another study⁴⁹, *cbp-1* knockdown alone shortened the lifespan of *C. elegans* (Fig. 4d,e), potentially due to the attenuated basal expression of diverse nuclear-encoded MSR transcripts (Fig. 1j).

We have previously shown that humans with Alzheimer's disease, as well as mouse and *C. elegans* models of Alzheimer's disease, are all typified by the induction of a cross-species conserved MSR transcript signature⁵⁰. Strikingly, further activation of these MSR pathways reduced A β proteotoxicity in cells, worms and transgenic mouse models of Alzheimer's disease⁵⁰. The GMC101 strain is a worm Alzheimer's disease model that expresses the human A β_{1-42} peptide in body-wall muscle cells⁵¹. Adults of GMC101 develop age-progressive paralysis and amyloid deposition after a temperature shift from 20 to 25°C. In these worms, *cbp-1* RNAi at 10% caused a severe developmental delay even in the absence of the disease-inducing temperature shift, phenocopying mitochondrial respiration mutants that rely on *cbp-1* for adaption, whereas the control CL2122 strain was not affected (Extended Data Fig. 4). Similar to *atfs-1* RNAi, *cbp-1* RNAi exacerbated A β aggregation in the GMC101 strain (Fig. 4f). In addition, *cbp-1* knockdown in GMC101 worms prominently repressed not only the classical UPR^{mt} transcripts (for example, *hsp-6*) but also many UPR^{mt} genes involved in proteolysis that only depend on CBP-1, but not ATFS-1 (for example, *asp-10*) (Fig. 1i,j and 4g). Interestingly, the transcripts of another branch of the MSR (that is, autophagy/mitophagy (for example, *sqst-1* and *dct-1*)) were conversely increased during *cbp-1* RNAi, suggesting a specific role of CBP-1 in regulating the UPR^{mt} branch of the MSR. Finally, *cbp-1* RNAi worsened the paralysis and completely blocked the beneficial effect of Dox, an antibiotic that inhibits mitochondrial translation and activates the MSR¹³, on the reduction of A β aggregates in GMC101 worms⁵⁰ (Fig. 4h,i). Together, these results indicate that CBP-1 is essential for the mitochondrial stress-induced immune response, lifespan extension and A β aggregation reduction in *C. elegans*.

CBP/p300 expression correlates with UPR^{mt} transcripts and lifespan. Next, we examined whether the role of CBP-1 in UPR^{mt} activation and MSR-associated beneficial effects is conserved in mammals. CBP expression in the spleen, pituitary gland, adrenal gland and eye positively correlated with *p300* expression in the C57BL/6J \times DBA/2J (BXD) mouse genetic reference population^{43,52} (www.genenetwork.org and Fig. 5a), confirming a complementary function of the two acetyltransferases^{35–37}. Their expression levels also correlated with transcript levels of *Kdm6b* and *Phf8*, the murine homologs of *jmjd-3.1* and *jmjd-1.2* (Fig. 5a). Moreover, in these tissues, CBP/p300 expression overall positively correlated with transcripts of UPR^{mt}-related genes^{10–12}, including the mitochondrial

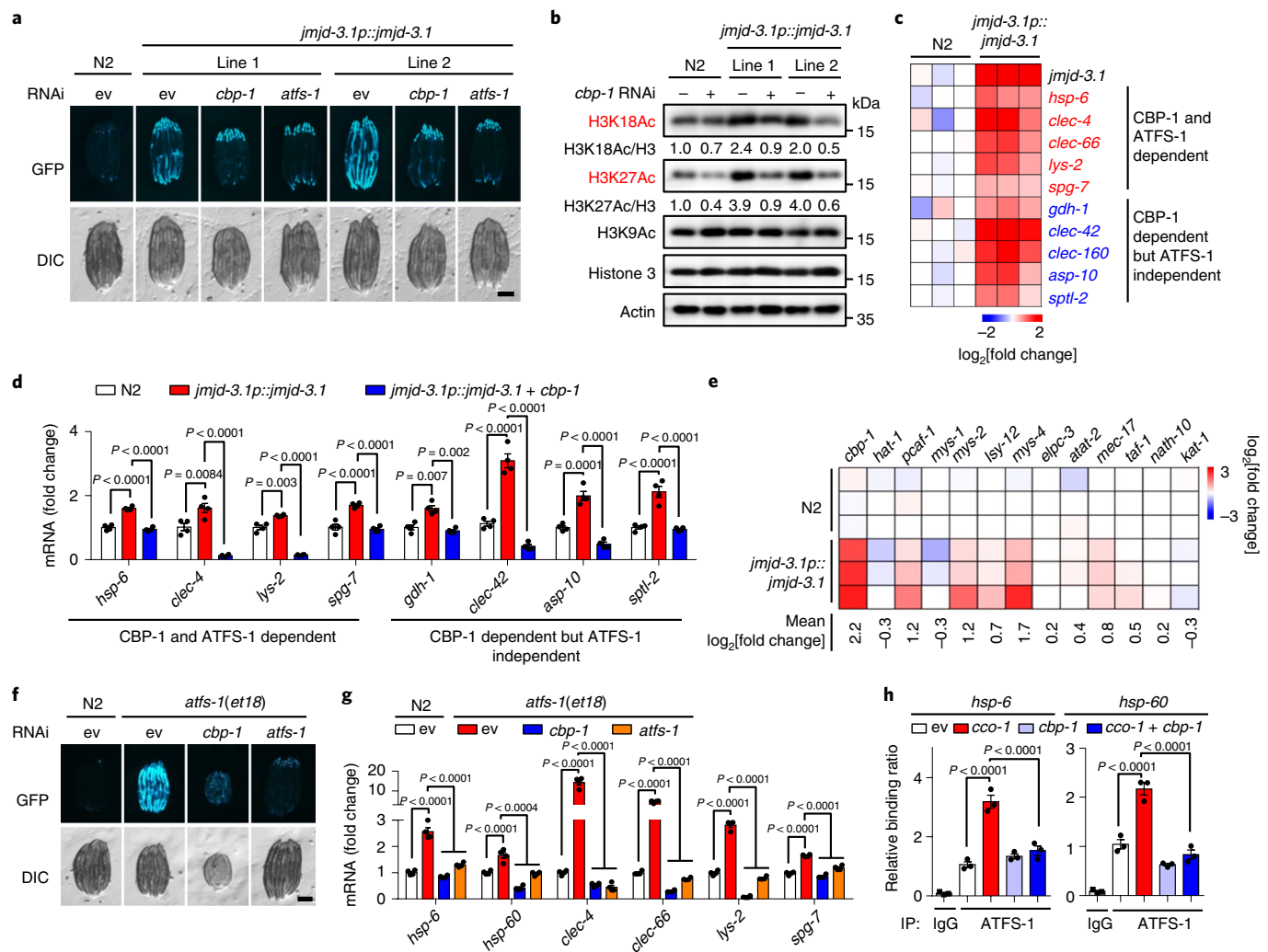


Fig. 3 | CBP-1 acts downstream of JMJD-3.1/JMJD-1.2 and upstream of ATFS-1 to support the expression of UPR^{mt} genes. **a**, *cbp-1* RNAi attenuates the UPR^{mt} activation induced by *jmjd-3.1* overexpression. Fluorescent micrographs of wild-type (N2) or two independent *hsp-6::gfp* worm lines carrying the integrated *jmjd-3.1p::jmjd-3.1* transgene fed with control, *cbp-1* (25%) or *atfs-1* (100%) RNAi are shown. **b**, *jmjd-3.1* overexpression increases H3K27Ac and H3K18Ac in a CBP-1-dependent manner. Western blots of wild-type or *jmjd-3.1* transgenic worms fed with control or *cbp-1* (25%) RNAi are shown. **c**, Heatmap showing strong upregulation of a representative set of CBP-1-dependent UPR^{mt} transcripts (\log_2 [fold change] values) in *jmjd-3.1* transgenic worms compared with wild-type (N2) worms²⁵. **d**, *jmjd-3.1* overexpression increases the expression of a representative set of CBP-1-dependent UPR^{mt} genes. RT-qPCR results of wild-type or *jmjd-3.1* transgenic worms fed with control or *cbp-1* (25%) RNAi ($n = 4$ biologically independent samples) are shown. **e**, Heatmap (\log_2 [fold change] values) showing the relative transcript levels of all putative KATs in wild-type and *jmjd-3.1p::jmjd-3.1* transgenic worms²⁵. **f**, *cbp-1* RNAi attenuates UPR^{mt} activation in the *atfs-1(et18)* mutant. Fluorescent micrographs of wild-type or *hsp-6::gfp* worms carrying the *atfs-1(et18)* mutant fed with control, *cbp-1* (25%) or *atfs-1* (100%) RNAi are shown. **g**, RT-qPCR results of the worms indicated in **f** ($n = 4$ biologically independent samples). **h**, *cbp-1* RNAi blocks the binding of ATFS-1 to the loci of UPR^{mt} genes. The results of ChIP-qPCR analysis of *hsp-6* and *hsp-60* in *atfs-1p::atfs-1::flag* worms fed with control, *cco-1* (50%) and/or *cbp-1* (25%) RNAi ($n = 3$ biologically independent samples) are shown. ChIP was performed using anti-Flag M2 beads. Error bars denote s.e.m. Statistical significance was determined by ANOVA followed by Tukey's post-hoc test. Scale bars (**a** and **f**), 0.3 mm.

proteases (*Lonp1*, *Yme11l* and *Spg7*), DNA-binding proteins (*Satb1* and *Ubl5*), mitochondrial chaperones (*Hsp61*, *Hspd1* and *Hspa9*) and asparagine synthetase, *Asns* (Fig. 5a). Similar correlation networks were also found in the hippocampus and hypothalamus of BXD mice (Extended Data Fig. 5a), as well as in the brain and prefrontal cortex of mice from a different genetic reference population, the inbred long-sleep \times inbred short-sleep (LXS) cohort⁵³ (Extended Data Fig. 5b). In accordance with the indispensable role of CBP-1 in MSR-associated health and lifespan regulation in *C. elegans* (Fig. 4), we observed positive correlations between lifespan and *CBP/p300* expression in the spleen, pituitary gland, adrenal gland, eye, hippocampus and hypothalamus of the BXD strains (Fig. 5b,c and Extended Data Fig. 5c).

Finally, in the human Genotype-Tissue Expression (GTEx) database⁵⁴, mRNA levels of *CBP/p300* positively correlated with *KDM6B*, *PHF8* and UPR^{mt} transcripts in many tissues, including the brain, hypothalamus, liver, heart, stomach, pancreas, kidney and small intestine, forming a systematic network (Fig. 5d). These observations suggest that *CBP/p300* probably plays an evolutionarily conserved role in MSR regulation across species from worms to humans.

A conserved role of CBP/p300 in MSR. To validate the strong connections between *CBP/p300* and UPR^{mt} activation in mammals, we challenged wild-type and *CBP/p300* knockout mouse embryonic fibroblasts (MEFs) with the mitochondrial stress inducer

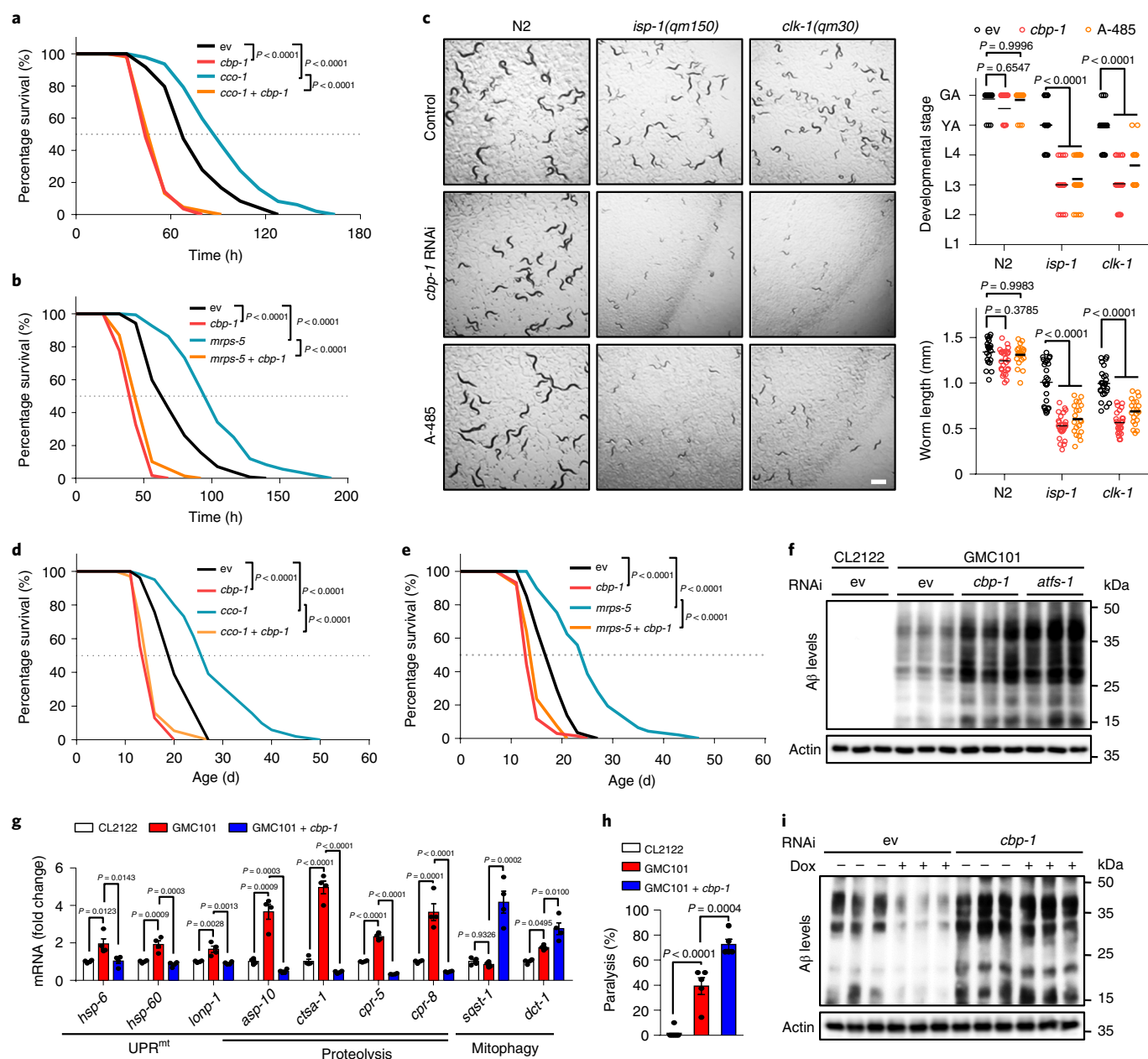


Fig. 4 | CBP-1 is essential for mitochondrial surveillance, MSR-associated immune response, lifespan extension and A β proteotoxicity reduction.

a, b. Impact of *cbp-1* knockdown on mitochondrial stress-induced *P. aeruginosa* resistance. The survival of worms fed with control (ev) or *cbp-1* (20%) RNAi, in combination with *cco-1* (50%) (**a**) or *mrps-5* (80%) (**b**) RNAi, and exposed to *P. aeruginosa*, is shown. **c.** Left: representative photos of wild-type (N2), *isp-1(qm150)* or *clk-1(qm30)* worms fed with control or *cbp-1* (10%) RNAi or treated with A-485 (10 μ M) since the maternal L4 stage. Scale bar, 1 mm. The developmental stage (top right) and body length (bottom right) of the F1 progeny were quantified at day 4 after hatching ($n=25$ worms for each condition). GA, gravid adult; L1-4, larval stages 1-4; YA, young adult. **d, e.** Impact of *cbp-1* knockdown on mitochondrial stress-induced lifespan extension. *cbp-1* RNAi attenuates lifespan extension induced by *cco-1* (50%) (**d**) or *mrps-5* (50%) (**e**) RNAi. RNAi targeting *cbp-1* occupies 20% (**d**) or 10% (**e**). **f, g.** Western blots of A β aggregation and actin levels (**f**), and transcript levels of selected genes measured by RT-qPCR ($n=4$ biologically independent samples) (**g**) of CL2122 or GMC101 worms fed with control, *cbp-1* (10%) or *atfs-1* RNAi. **h.** Percentage of paralysis of CL2122 or GMC101 worms fed with control or *cbp-1* (10%) RNAi at day 5 of adulthood ($n=5$ independent experiments). **i.** Impact of *cbp-1* knockdown on mitochondrial stress-induced A β proteotoxicity reduction. Western blots of A β aggregation and actin in GMC101 worms fed with control or *cbp-1* (10%) RNAi with or without Dox (15 μ g ml⁻¹) treatment are shown. Error bars denote s.e.m. Statistical significance was determined by ANOVA followed by Tukey's post-hoc test (**c, g** and **h**) or log-rank test (**a, b, d** and **e**).

Dox^{13,36}. Dox induced many UPR^{mt} transcripts, such as *Hspd1*, *Hspa9*, *Lonp1* and *Asns*, a response that was remarkably blocked by *CBP/p300* knockout (Fig. 6a). RNA-seq analysis revealed that 327 transcripts were upregulated ($\log_2[\text{fold change}] > 0.5$; adjusted $P < 0.05$) and 245 transcripts were downregulated ($\log_2[\text{fold}$

change] < -0.5 ; adjusted $P < 0.05$) in wild-type MEFs upon Dox treatment (Extended Data Fig. 6a,b and Supplementary Table 5). In contrast, only 38 upregulated and 58 downregulated transcripts were detected in *CBP/p300*^{-/-} MEFs (Extended Data Fig. 6b). Importantly, up to 197 (60.2%) of the 327 Dox-induced transcripts

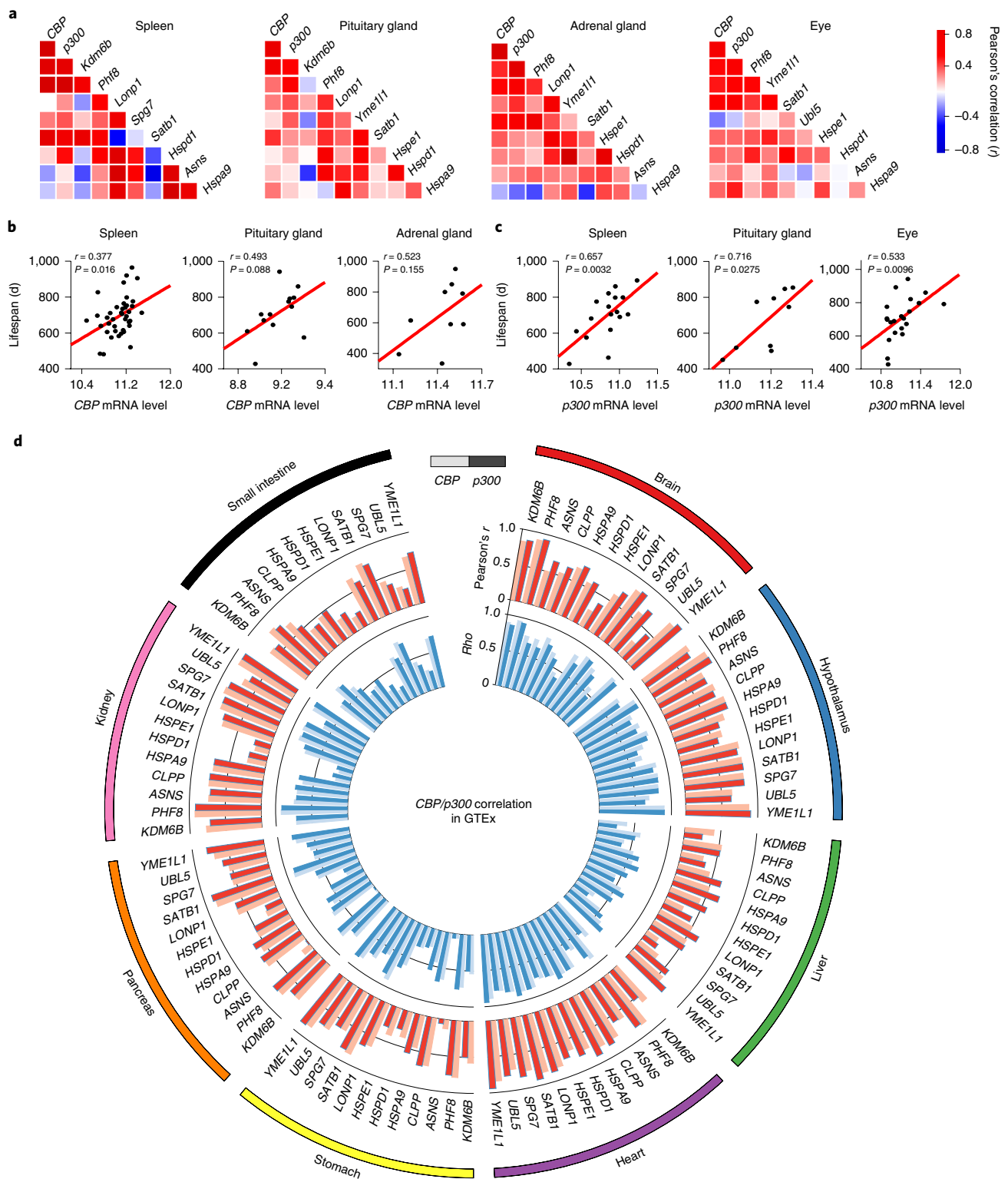


Fig. 5 | Expression of *CBP/p300* positively correlates with *UPR^{mt}* transcripts and longevity in mouse and human populations. **a, Pearson's correlation co-expression heatmap for *CBP*, *p300*, *Kdm6b*, *Phf8* and *UPR^{mt}* genes in the spleen, pituitary gland, adrenal gland and eye of the BXD mouse genetic reference population^{43,52}. Positive and negative correlations are indicated in red and blue, respectively. The intensity of the colors corresponds to the correlation coefficient. **b**, Positive correlations between lifespan and *CBP* transcript levels in the spleen, pituitary gland and adrenal gland of BXD mice (Pearson's r ; two sided). **c**, Positive correlations between lifespan and *p300* transcript levels in the spleen, pituitary gland and eye of BXD mice (Pearson's r ; two sided). **d**, Circos plot of the expression correlations between *CBP/p300* transcripts and *UPR^{mt}* gene transcripts in the brain (cerebellar hemisphere), hypothalamus, liver, heart (left ventricle), stomach, pancreas, kidney and small intestine of human samples derived from the GTEx database (version 8)⁵⁴. The red bar ring shows the Pearson's correlation coefficients (r) between *UPR^{mt}* gene transcripts and *CBP* (light red) or *p300* (dark red). The blue bar ring shows the Spearman's rank correlation coefficients (Rho) between *UPR^{mt}* gene transcripts and *CBP* (light blue) or *p300* (dark blue). All correlations were found to be positive.**

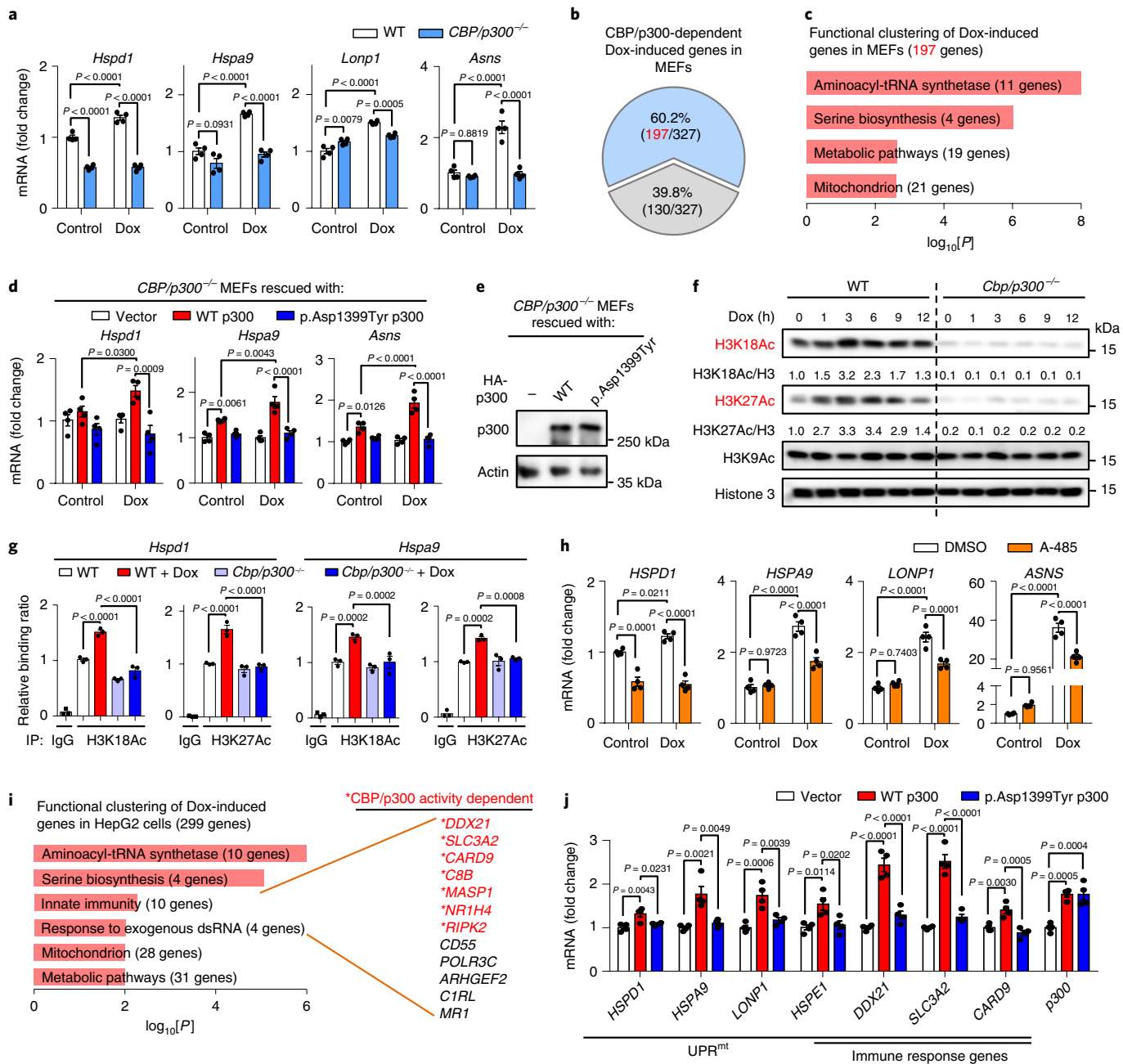


Fig. 6 | Functions of CBP/p300 in UPR^{mt} activation are conserved in mammals. **a**, Knockout of *CBP/p300* attenuates Dox-induced transcription of key UPR^{mt} genes in MEFs. The RT-qPCR results of wild-type (WT) and *CBP/p300*^{-/-} MEFs treated with or without Dox (30 μg ml⁻¹) for 24 h (*n* = 4 biologically independent samples) are shown. **b**, Diagram of the UPR^{mt} genes that are dependent (blue) or independent (grey) on CBP/p300 for induction upon Dox treatment in MEFs, according to the RNA-seq data. **c**, Functional clustering of the 197 genes indicated in **b**. **d, e**, Transcripts (*n* = 4 biologically independent samples) (**d**) and protein levels (**e**) of *CBP/p300*^{-/-} MEFs reconstituted with empty vector, wild-type p300 or the p.Asp1399Tyr acetyltransferase activity-defective variant of p300, after control or Dox (30 μg ml⁻¹) treatment for 24 h. **f**, Western blots showing time-dependent changes of H3K18Ac and H3K27Ac in wild-type and *CBP/p300*^{-/-} MEFs treated with Dox (30 μg ml⁻¹) for 0–12 h. **g**, *CBP/p300* is essential for Dox-induced H3K18Ac and H3K27Ac at the promoters of UPR^{mt} genes (for example, *Hspd1* and *Hspa9*). The results of ChIP-qPCR analysis of *Hspd1* and *Hspa9* in wild-type and *CBP/p300*^{-/-} MEFs treated with or without Dox (30 μg ml⁻¹) for 3 h (*n* = 4 biologically independent samples) are shown. ChIP was performed using antibodies to H3K18Ac or H3K27Ac. **h**, The CBP/p300 acetyltransferase activity inhibitor A-485 strongly suppresses Dox-induced transcription of key UPR^{mt} genes in HepG2 cells. The RT-qPCR results of HepG2 cells pretreated with DMSO or A-485 (5 μM) for 1 h and then co-treated with or without Dox (30 μg ml⁻¹) for 24 h (*n* = 4 biologically independent samples) are shown. **i**, Functional clustering of the 299 genes upregulated upon Dox treatment (30 μg ml⁻¹; 24 h) in human HepG2 cells analyzed by RNA-seq. The CBP/p300 activity dependency was evaluated by the impact of A-485 treatment. For a subset of 14 genes in the categories indicated by orange brackets, 7 out of 12 genes were CBP/p300 activity-dependent (indicated in red). dsRNA, double-stranded RNA. **j**, RT-qPCR results of HepG2 cells overexpressing empty vector, wild-type p300 or the acetyltransferase activity-defective variant p.Asp1399Tyr (*n* = 4 biologically independent samples). Error bars denote s.e.m. Statistical significance was determined by ANOVA followed by Tukey’s post-hoc test.

in wild-type MEFs were dependent on CBP/p300 for induction (Fig. 6b). These Dox-induced and CBP/p300-dependent transcripts were enriched for the following categories: aminoacyl-tRNA synthetase, confirming a close link between mRNA translation and the UPR^{mt} (refs. 21,55); serine biosynthesis, including *Phgdh*, *Psat1*, *PspH* and *Shmt2* (refs. 19,56); and metabolic and mitochondrial pathways (for example, *Eno1b* and *Timm10*) (Fig. 6c and Extended Data Fig. 6c). Similar gene sets were also recently reported to be induced by other MSR inducers, such as carbonyl cyanide *m*-chlorophenyl hydrazone and oligomycin, in different mammalian cells^{22,23}. It is also noteworthy that Dox-induced expression of both *Atf4* and *Atf5*, two key transcriptional regulators of the UPR^{mt} (refs. 19,20), was heavily dependent on CBP/p300 (Extended Data Fig. 6c), suggesting a commanding role of CBP/p300 in UPR^{mt} activation. In addition, reconstitution of wild-type p300, but not a p300 acetyltransferase activity-defective mutant, restored Dox-induced UPR^{mt} activation in *CBP/p300*^{-/-} MEFs (Fig. 6d,e), confirming that the catalytic activity of CBP/p300 is indispensable for this stress response.

In line with increased CBP/p300-mediated histone acetylation during mitochondrial perturbations in *C. elegans* (Fig. 2a–c), H3K18Ac and H3K27Ac levels peaked at 3–6 h of Dox treatment in wild-type MEFs, and this was substantially attenuated in *CBP/p300*^{-/-} MEFs (Fig. 6f). Meanwhile, H3K9Ac was not affected by the knockout of *CBP/p300* (Fig. 6f). ChIP–qPCR analysis further revealed that *CBP/p300* is essential for Dox-induced increases in H3K18Ac and H3K27Ac levels at the promoters of prototypical UPR^{mt} genes (for example, *Hspd1* and *Hspa9*) (Fig. 6g).

Liver is the central hub for metabolism and we have previously found that hepatocytes respond robustly to Dox treatment¹³. We thus further tested the impact of Dox treatment in the human hepatoma cell line HepG2. Similar to the effect of *CBP/p300* knockout, the induction of multiple prototypical UPR^{mt} transcripts upon Dox treatment was abolished by the CBP/p300 KAT activity inhibitor A-485 (Fig. 6h). RNA-seq analysis revealed that the expression of a much smaller number of transcripts was altered upon Dox treatment in A-485-treated cells, compared with that in control cells (Extended Data Fig. 6d,e). Moreover, Dox treatment induced 299 transcripts (log₂[fold change] > 0.5; adjusted *P* < 0.05), and the induction of 163 (54.5%) of them was abrogated by A-485 (Extended Data Fig. 6f and Supplementary Table 6). Notably, in addition to the Gene Ontology terms found in MEFs (for example, aminoacyl-tRNA synthetase and mitochondrion), the Dox-induced transcripts in HepG2 cells were also enriched for innate immunity and response to exogenous double-stranded RNA, containing 12 genes (two genes belonged to both terms), and seven of them were dependent on CBP/p300 activity for induction (Fig. 6i and Supplementary Table 6). Finally, forced expression of wild-type p300, but not the KAT activity-defective mutant of p300, is sufficient to induce the expression of UPR^{mt} and Dox-induced immune response genes (for example, *DDX21* and *SLC3A2*) in HepG2 cells (Fig. 6j). Taken together, these results point to a conserved and central role of CBP/p300 in MSR regulation in mammals.

Discussion

Here, by employing multilayered genetic and pharmacological approaches applied to *C. elegans*, mouse and human populations and cell lines, we provide strong evidence that CBP-1 (or the mammalian equivalent CBP/p300) acts downstream of the demethylases JMJD-3.1 and JMJD-1.2 (or mammalian KDM6B/PHF8), switching the transcription-repressive histone methylation marks (for example, H3K27Me3) to the transcription-active acetylation marks (for example, H3K27Ac), and thereby relays the mitochondrial stress signal to the transcriptional induction of diverse UPR^{mt} genes in *C. elegans* as well as in mammals (Fig. 7). Notably, many of the CBP-1- or CBP/p300-dependent UPR^{mt} effectors positively contribute to mitochondrial function recovery, improved immune response,

enhanced proteostasis against A β aggregation, and lifespan extension. In support of these findings, changes in CBP/p300 function tightly associate with multiple aging/mitochondrial-related diseases, including Alzheimer's disease and Huntington's disease^{57–59}, and forced expression or pharmacological activation of CBP/p300 is sufficient to ameliorate neurodegenerative phenotypes in both mouse and *Drosophila* Alzheimer's disease models^{60–62}.

How CBP-1 or CBP/p300, as well as the histone demethylases, sense mitochondrial stress remains an important direction for future work. One possibility is that CBP-1 itself is a downstream target that is activated in response to mitochondrial stress, as evidenced by increased *cbp-1* expression after *cco-1* and *mrps-5* silencing (Extended Data Fig. 2c), and after *jmjd-3.1* overexpression (Fig. 3e). Changes in mitochondrial metabolism may also modulate the levels of acetyl-CoA, which acts as a substrate for the acetyltransferase activity of KATs including CBP/p300 (refs. 30,32,63).

Of note, despite the fact that we mainly focused on the regulation of H3K27Ac and H3K18Ac upon mitochondrial stress, due to the availability of the reagents, it is very likely that a similar regulatory mechanism exists as well for other CBP-1- or CBP/p300-mediated histone acetylation sites^{32,37} (for example, H4K5Ac; Extended Data Fig. 3a), which could also positively contribute to chromatin decompaction and transcriptional reactivation⁴⁴. Moreover, CBP/p300 may also affect mitochondrial function and stress resistance by targeting proteins besides histones. As a first attempt in this direction, we investigated whether ATFS-1 could be acetylated by CBP-1. CBP-1 could indeed acetylate ATFS-1 both in vivo and in vitro (Extended Data Fig. 7a,b). Using mass spectrometry, we identified three acetylation sites in ATFS-1 (Extended Data Fig. 7c). Additionally, we investigated which class of histone deacetylase (HDAC) is responsible for the deacetylation of ATFS-1. Using trichostatin A (TSA; a class I/II HDAC inhibitor) and nicotinamide (NAM; a class III HDAC inhibitor), we found that HDACs belonging to at least two different classes participate in the deacetylation of ATFS-1 (Extended Data Fig. 7d). Furthermore, it has been reported that peroxisome proliferator-activated receptor- γ coactivator-1 α can be acetylated by p300 and deacetylated by Sirt1, serving as an important switch controlling mitochondrial biogenesis and function^{64,65}. In another study, p300 was identified as a binding partner for ATF4 and could enhance ATF4-mediated transcriptional activation through a mechanism independent of its acetyltransferase activity⁶⁶.

In addition to the indispensable role of CBP-1 or CBP/p300 in MSR, we have noticed that the basal expression of some UPR^{mt} transcripts also decreased after *cbp-1* silencing, *CBP/p300* knockout or CBP/p300 activity inhibition (Figs. 1j and 6a,h and Supplementary Tables 1 and 5), suggesting that CBP/p300 functions in maintaining basal UPR^{mt} activity as well. Nevertheless, the distinction between basal and stress conditions is somehow artificial, especially considering that organisms and cells are constantly exposed to multiple cues, and different wild *C. elegans* strains differ with respect to the level of UPR^{mt} activation under basal conditions⁶⁷. Moreover, it is likely that some UPR^{mt} genes controlled by CBP-1 or CBP/p300 may also contribute to basal mitochondrial function. For example, the chaperone *hsp-60* and its mouse ortholog *Hspd1*, which demonstrated decreased basal H3K18Ac/H3K27Ac enrichment, ATFS-1 binding and mRNA expression upon *cbp-1* RNAi or *CBP/p300* suppression (Figs. 2k, 3h and 6a,g,h), have been reported to be essential for mitochondrial homeostasis even in the basal state^{27,68}. It is also noteworthy that we detected increased CBP-1 or CBP/p300-mediated acetylation marks during mitochondrial stress in both promoter and coding regions for a large set of genes (Extended Data Fig. 3f and Supplementary Table 3). According to a systematic study on mapping the global histone acetylation patterns to gene expression in yeast⁶⁹, hyperacetylation of both intergenic and coding regions genome wide at histones H3K18 and H3K27 is robustly

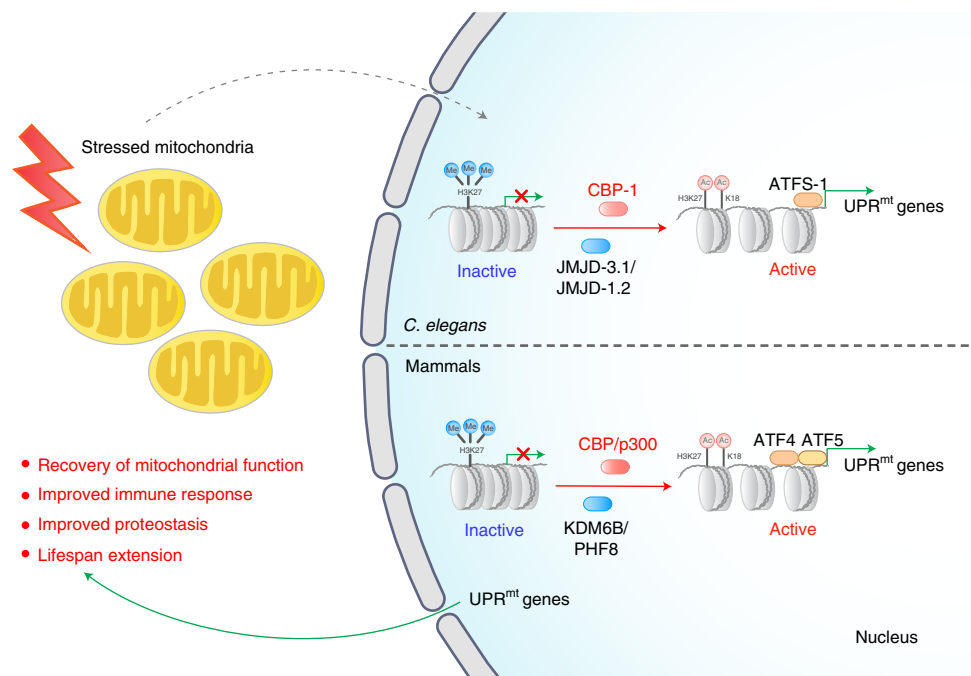


Fig. 7 | Model for CBP-1- or CBP/p300-mediated regulation of MSR and longevity. When the mitochondria are stressed in response to various intracellular or extracellular stimuli, CBP-1 (or mammalian CBP/p300) acts downstream of the demethylases JMJD-3.1 and JMJD-1.2 (or mammalian KDM6B and PHF8), switching the transcription-repressive histone methylation marks (for example, H3K27Me3) to the transcription-active acetylation marks (for example, H3K27Ac), and thereby relays the mitochondrial stress signal to the transcriptional induction of diverse UPR^{mt} genes in *C. elegans* as well as in mammals. Many of these UPR^{mt} effectors play positive roles in the recovery of mitochondrial function, improved immune response and proteostasis, and lifespan extension.

correlated with active transcription. It is therefore likely that acetylation marks in both the promoter and coding regions in our context may contribute to transforming the condensed chromatin into a more relaxed structure and thus facilitate transcription^{29,30,32,44}.

Altogether, by applying genetic and pharmacological LOF approaches, combined with bioinformatic and mechanistic studies, we identified the acetyltransferase CBP-1 as an essential regulator for activation of the MSR and, in particular, the UPR^{mt}. The beneficial effects on pathogen infection resistance, protein aggregation reduction and lifespan extension caused by mitochondrial perturbations are almost completely dependent on CBP-1 in *C. elegans*. Furthermore, systematic correlation analysis in mouse and human populations, as well as LOF studies in mammalian cells, indicate that functions of CBP/p300 in UPR^{mt} regulation and longevity are also conserved in mammals. Our results thus reveal an evolutionarily conserved mechanism that coordinates the multiple layers of UPR^{mt} regulators to systematically activate the stress responses, defend mitochondrial function and promote health and longevity. Further studies will have to define whether genetically or pharmacologically targeting these CBP/p300-driven MSR pathways can have therapeutic applications against mitochondrial-related diseases, pathogen infections and aging.

Methods

***C. elegans* strains.** The Bristol strain (N2) was used as the wild-type strain. *SJ4100* (*zcls13[hsp-6p::GFP]*), *MQ887* (*isp-1(qm150)IV*), *MQ130* (*clk-1(qm30) III*), *QC118* (*atfs-1(et18)*), *OP675* (*atfs-1::TY1::EGFP::3xFLAG*), *GMC101* (*dvlIs100 [unc-54p::A-beta-1-42::unc-54 3'-UTR + mtl-2p::GFP]*) and *CL2122* (*dvlIs15 [(pPD30.38) unc-54(vector) + (pCL26) mtl-2::GFP]*) were obtained from the Caenorhabditis Genetics Center (Minneapolis, Minnesota). Strains with *jmjd-3.1* overexpression line 1 *AUW3* (N2, *epfIs3[myo-2p::cfp, jmjd-3.1p::jmjd-3.1]; zcls13[hsp-6p::gfp]V*) and line 2 *AUW4* (N2, *epfIs4[myo-2p::cfp, jmjd-3.1p::jmjd-3.1]; zcls13[hsp-6p::gfp]V*) were described previously²⁵. The strain *atfs-1(et18); zcls13[hsp-6p::GFP]* was generated by crossing the *SJ4100* (*zcls13[hsp-6p::GFP]*) males with the *QC118* (*atfs-1(et18)*) early L4 hermaphrodites. Worms were cultured at 20 °C and fed

with *Escherichia coli* OP50 on nematode growth media (NGM) plates unless otherwise indicated.

RNA interference. Bacterial feeding RNAi experiments were performed as described¹³. RNAi clones were used from either the Ahringer or Vidal library and verified by sequencing. Double RNAi experiments were carried out by mixing bacterial cultures normalized to their optical densities (OD₆₀₀) before seeding onto NGM plates.

The alternative *cbp-1* RNAi clone (*cbp-1* RNAi₂) was constructed by PCR amplification of *cbp-1* complementary DNA (cDNA) from total RNA with the following primers: *cbp-1*_RNAi₂_632_Fw (5'-CTCGAGGGTGTGGAAGGTGGACGTAG-3') and *cbp-1*_RNAi₂_632_Rv (5'-AGATCTTCCATTGGGCGCTTGATGAT-3'). The PCR product was then ligated into the L4440 empty vector and transformed into *E. coli* HT115 competent cells. The *cbp-1* RNAi clone from the Ahringer library (*cbp-1* RNAi₁) was used for all of the experiments related to *cbp-1* RNAi unless otherwise indicated.

Lifespan experiments were performed at 20 °C as described previously⁷⁰. Briefly, 75–100 animals were used per condition and scored every other day, and those disappeared or exploded at the vulva were censored. All RNAi treatment for lifespan started at the maternal L4 stage.

Induction of the UPR^{mt}. For RNAi-induced UPR^{mt}, RNAi bacteria were grown in lysogeny broth containing 25 mg ml⁻¹ carbenicillin at 37 °C overnight. The bacteria were then seeded onto 6-cm NGM plates with 2 mM isopropyl β-D-1-thiogalactopyranoside. Dried plates were kept at room temperature overnight to allow isopropyl β-D-1-thiogalactopyranoside induction of double-stranded RNA expression. L4 worms or synchronized worm eggs were raised on the RNAi plates at 20 °C. The F0 worms were then removed the next day if L4 worms were seeded the day before. Fluorescent images with the same exposure time for each condition were taken after 2–3 d. For antimycin A or Dox-induced UPR^{mt}, antimycin A (A8674; Sigma–Aldrich) with a final concentration of 2.5 μM or Dox (D9891; Sigma–Aldrich) with a final concentration of 30 μg ml⁻¹ was added to the NGM just before pouring the plates.

RNA extraction and RNA-seq analysis. For worm samples, worms were synchronized by bleaching. Synchronized worm eggs were plated in NGM plates under the described conditions and raised at 20 °C. Worms were harvested after 2 d (at the L4/young adult stage), washed with M9 buffer three times to remove the bacteria, then snap frozen in liquid nitrogen. On the day of the extraction, 1 ml TriPure Isolation Reagent (11667165001; Roche) was added to each tube.

The samples were then frozen and thawed quickly eight times with liquid nitrogen and a water bath to rupture the cell membranes. RNA was then extracted using a column-based kit from Macherey–Nagel (740955.250). For mammalian cell samples, cells were directly dissolved in 1 ml TriPure Isolation Reagent and extracted using the kit from Macherey–Nagel (740955.250). RNA-seq was performed by the Beijing Genomics Institute with the BGISEQ-500 platform.

RNA-seq data analysis for worm samples was performed using the R version 3.6.3 (<https://www.r-project.org/>). Briefly, after sequencing on the BGISEQ-500 platform, the raw reads were filtered by removing adaptor sequences, contamination and low-quality (Phred quality < 20) reads. FastQC⁷¹ was used to verify the quality of the sequence data. Sequenced reads were mapped to the worm genome *Caenorhabditis elegans*. WBcel235.89 with STAR aligner version 2.6.0a⁷². Reads were counted using htseq-count version 0.10.0 (ref. ⁷³), using the following flags: -f bam -r pos -s no -m union -t exon -i gene_id. Differential expression of genes was calculated using limma-voom^{74,75}. The genes with a Benjamini–Hochberg adjusted *P* value of < 0.05 were defined as statistically significant. Genes with significantly upregulated expression ($\log_2[\text{fold change}] > 0.5$; adjusted *P* < 0.05) in the *cco-1* RNAi condition that were then downregulated by more than 25% of the $\log_2[\text{fold change}]$ after *cbp-1* or *atfs-1* RNAi co-treatment, compared with the $\log_2[\text{fold change}]$ of the *cco-1* RNAi condition, were considered CBP-1 or ATFS-1 dependent. Genes with significantly downregulated expression ($\log_2[\text{fold change}] < -0.5$; adjusted *P* < 0.05) were defined as downregulated genes. For MEFs or human HepG2 cell samples, a similar analysis procedure was used except that the *Mus musculus*.GRCh38.95 or *Homo sapiens*.GRCh38.95 genome was used for mapping. Genes with upregulated expression ($\log_2[\text{fold change}] > 0.5$; adjusted *P* < 0.05) in the Dox treatment condition that were then downregulated by more than 25% of the $\log_2[\text{fold change}]$ after *CBP/p300* knockout or A-485 treatment, compared with the $\log_2[\text{fold change}]$ of the wild-type Dox condition, were considered CBP/p300 dependent or CBP/p300 activity dependent. Functional clustering was performed using the Database for Annotation, Visualization and Integrated Discovery⁷⁶. Heatmaps were generated using Morpheus (<https://software.broadinstitute.org/morpheus>).

Quantitative PCR with reverse transcription (RT–qPCR). Worms were raised and total RNA was isolated as described for the RNA-seq studies. cDNA was then synthesized from total RNA using the Reverse Transcription Kit (205314; Qiagen). RT–qPCR was performed using the LightCycler 480 SYBR Green I Master kit (04887352001; Roche). The primers used for RT–qPCR are listed in Supplementary Table 7. Primers for worm *pmp-3*, mouse *Actin* and human *ACTB* were used as normalization controls.

Western blotting. For worm samples, proteins were extracted as described previously¹³. Western blotting was performed with antibodies against green fluorescent protein (GFP) (1:1,000; 2956; CST), actin (1:2,000; A5441; Sigma–Aldrich), H3K18Ac (1:1,000; 07-354; Merck), H3K27Ac (1:1,000; ab4729; Abcam), H3K9Ac (1:1,000; 06-942; Merck), H3K4Ac (1:1,000; Ab176799; Abcam), histone 3 (1:1,000; 9715; CST), tubulin (1:2,000; T5168; Sigma–Aldrich), H3K27Me3 (1:1,000; 07-449; Millipore), H3K27Me2 (1:1,000; ab24684; Abcam), H3K27Me1 (1:1,000; 07-448; Millipore), H3K9Me1 (1:1,000; 07-450; Millipore), H3K4Me3 (1:1,000; 07-473; Millipore), histone 4 (1:1,000; sc-10810; Santa Cruz), H4K5Ac (1:1,000; ab51997; Abcam), β -amyloid 1–16 (6E10) (1:1,000; 803001; BioLegend), HA-tag (1:2,000; 3724; CST), Flag-tag (1:1,000; F7425; Sigma–Aldrich), Myc-tag (1:2,000; sc-40; Santa Cruz), GST-tag (1:1,000; 2625; CST), AcK (1:1,000; 9441; CST), AcK (1:1,000; 9814; CST) and HRP-labelled anti-rabbit (7074; CST) and anti-mouse (7076; CST) secondary antibodies.

ChIP and ChIP-seq of worms. ChIP of worms was performed as described⁷⁷, with slight modifications. Briefly, worms were synchronized by bleaching. Synchronized worm eggs were plated in NGM plates under the described conditions and raised at 20°C. Worms were harvested after 2 d (at the L4/young adult stage) and washed with M9 buffer three times. Worms were then fixed with 1% formaldehyde in phosphate-buffered saline for 30 min and quenched by glycine. Immunoprecipitations were carried out using antibodies against H3K18Ac (1:100; 07-354; Merck) or H3K27Ac (1:100; ab4729; Abcam). For ChIP of ATFS-1, the *OP675 (atfs-1::TY1::EGFP::3xFLAG)* worm strain and anti-Flag M2 beads (A2220; Sigma–Aldrich) were used. The primers used for ChIP–qPCR are listed in Supplementary Table 7.

For ChIP-seq, DNA fragments were sequenced using the BGISEQ-500 platform. Data analysis was performed using R version 3.6.3 (<https://www.r-project.org/>). FastQC⁷¹ was used to verify the quality of the sequence data. Alignment was performed against the *C. elegans* genome *Caenorhabditis elegans*. WBcel235.89 following the Bowtie 2 (version 2.3.5)⁷⁸ manual guidelines with default parameters. SAMtools (version 1.4.1)⁷⁹ was used to sort, filter and index the obtained alignments. Peak calling was then performed using MACS2 (version 2.1.2)⁸⁰ against the default Poisson distribution to generate raw counts for each sample, or between samples of interest for comparison. The peak scores between treatment and control for each histone modification were generated with an associated FDR value (a default FDR value of 0.05). The quality of alignment and peaks was assessed using CHIPQC (version 1.18.2)⁸¹ before proceeding with the analysis.

Read counts per peak were obtained using BEDTools (version 2.26.0)⁸² and SAMtools (version 1.4.1)⁷⁹ packages. Intersection between sets and their associated *P* values was computed using the SuperExactTest7 (version 1.0.6)⁸³ package. Genome tracks were revealed by Integrative Genomics Viewer (version 2.8.0)⁸⁴. The two tracks were shown with the same total count range between basal and mitochondrial stress conditions for each gene.

***P. aeruginosa* infection assay.** The *P. aeruginosa* PA14 slow-killing assay was performed as described⁸⁵. Briefly, *P. aeruginosa* overnight cultures were seeded onto slow-killing NGM agar plates with 0.35% peptone. Plates were allowed to dry for 20 min at room temperature, then incubated at 37°C for 24 h and allowed to equilibrate at 25°C for another 24 h. Synchronized worm eggs were raised on RNAi bacteria, as indicated in the figure captions, until they reached the L4 stage. The worms were then transferred to *P. aeruginosa* slow-killing plates and counted every 12 h. Animals were scored as dead if they failed to respond when gently punched with a worm picker. In total, 80–100 worms were used for each condition, and those disappeared or exploded at the vulva were censored. Each experiment was performed at least twice, and the log-rank (Mantel–Cox) statistical test was used to calculate *P* values.

Cell culture and drug treatment. HepG2 cells were obtained from the American Type Culture Collection. Cells were validated to be free of *Mycoplasma* contamination and maintained in Dulbecco's modified Eagle's medium containing 4.5 g glucose per liter and 10% fetal bovine serum. Immortalized *Crebbp*^{fl/fl}; *Ep300*^{fl/fl} MEFs stably expressing Cre-ERT2 were kindly provided by P. K. Brindle⁸⁶. The floxed *CBP/p300* alleles were deleted as previously described³⁷. Briefly, *Crebbp*^{fl/fl}; *Ep300*^{fl/fl} MEFs were treated with 2 μ M 4-hydroxy-tamoxifen (H7904; Sigma–Aldrich), the media was changed and fresh 4-OHT was added every 12 h for 2 d. Cells were cultured for an additional 1 d to allow for complete depletion of CBP/p300 protein. For transfection, plasmids expressing human full-length wild-type p300 (89094; Addgene) and the p300 acetyltransferase activity-defective mutant (89095; Addgene)⁸⁶ were purchased from Addgene and transfected with Lipofectamine 3000 Reagent (L3000015; Thermo Fisher Scientific). The CBP/p300 acetyltransferase inhibitor A-485 (6387; Tocris) and bromodomain inhibitor PF-CBP1 (S8180; Selleck Chemicals) were dissolved in dimethyl sulfoxide (DMSO) and treated with final concentrations as described in the figure captions. For the treatment of worms with CBP/p300 inhibitors, A-485 or PF-CBP1 was added to the NGM agar medium, with final concentrations as indicated, just before pouring the plates.

ATFS-1 acetylation analysis. For in vivo analysis, plasmids expressing full-length ATFS-1 or the HAT domain of CBP-1 (amino acids 803–1620) were created by PCR amplification from total worm cDNA and verified by sequencing. Transfection was performed with Lipofectamine 3000 Reagent (L3000015; Thermo Fisher Scientific) in HEK293T cells. TSA (5 μ M; T8552; Sigma–Aldrich) and/or NAM (10 mM; N0636; Sigma–Aldrich) were added to the culture medium 8 h before harvesting. For in vitro analysis, the HAT domain of CBP-1 (amino acids 803–1620) was subcloned to the GST-tag-containing pGEX-4T-1 vector and purified from the BL21 bacteria. An in vitro acetylation assay was carried using 50- μ l reactions containing 50 mM HEPES (pH 8.0), 10% glycerol, 1 mM dithiothreitol, 1 mM phenylmethylsulfonyl fluoride, 5 μ M TSA, 10 mM NAM, 100 μ M acetyl-CoA, immune-purified ATFS-1 from HEK293T cells and GST–HAT–CBP-1. After incubation at 30°C for 1 h, the reaction was stopped by the addition of 10 μ l 5 \times sodium dodecyl sulfate sample buffer. The samples were then subjected to sodium dodecyl sulfate polyacrylamide gel electrophoresis and western blotting.

Bioinformatics analyses. All BXD, LXS and GTEX transcriptome results for bioinformatics analyses were downloaded from GeneNetwork (<http://www.genenetwork.org>) and analyses were performed as described in previous studies^{43,52,53}. The BXD transcriptome datasets used to establish genetic correlations were UTHSC Affy MoGene 1.0 ST Spleen (Dec10) RMA Males, INIA_Pituitary_RMA_M_0612, INIA Adrenal Affy MoGene 1.0 ST (Jun12) RMA Males, Eye M430v2 (Sep08) RMA, Hippocampus Consortium M430v2 (Jun06) RMA and INIA Hypothalamus Affy MoGene 1.0 ST (Nov10) Male. The IDs for the lifespan datasets were 12564, 17475, 18435, 19422 and 19424. The LXS transcriptome datasets used were UCAMC LXS Whole Brain Saline RNA Sequence (Feb16) FPKM and VCU LXS PFC Sal M430A 2.0 (Aug06) RMA. For human genetic correlation analyses, the GTEX v8 All Tissues dataset was used⁸⁴. Pearson's *r* was used for measuring the correlations. Correlation heatmaps were generated using Morpheus (<https://software.broadinstitute.org/morpheus>). The Circos plot was generated using Circos (<http://www.circos.ca>)⁸⁷.

Statistics and reproducibility. No statistical methods were used to predetermine sample sizes but our sample sizes are similar to those reported in previous publications^{13,50,70}. Samples were allocated to groups or treatments randomly, and steps were taken to avoid batch effects. Experimental conditions were not blinded. However, data analysis was performed blind whenever possible. No data were excluded from the analysis, except for the *C. elegans* lifespan and survival

experiments (the reasons for censoring, which were pre-established before the beginning of the experiment^{13,70}, were the exploded vulva phenotype or worms that crawled off the plate). All individual data points are shown in the figures. The data distribution was assumed to be normal but this was not formally tested. All of the experiments, particularly the representative micrographs shown in Figs. 1a–e and 3a,f and Extended Data Fig. 1b–d,f–h,k–n, were repeated at least twice, and similar results were found. Survival analyses were performed using the Kaplan–Meier method and the significance of differences between survival curves was calculated using the log-rank (Mantel–Cox) test. Differences between two groups were assessed using two-tailed unpaired Student's *t*-tests. Analysis of variance (ANOVA) followed by Tukey's post-hoc test (one-way ANOVA for comparisons between groups; two-way ANOVA for comparisons of the magnitude of changes between different groups from different cell lines or treatments) was used when comparing more than two groups. *P* values were adjusted for multiple comparisons. GraphPad Prism 6 was used for all statistical analyses. Fiji (version 1.47b) was used to quantify the western blots shown in Fig. 2a–c and Extended Data Fig. 3a.

Reporting Summary. Further information on research design is available in the Nature Research Reporting Summary linked to this article.

Data availability

The RNA/DNA sequencing datasets have been deposited in the National Center for Biotechnology Information Gene Expression Omnibus database with the accession numbers GSE131611 (for worm RNA-seq), GSE148328 (for worm ChIP-seq), GSE131613 (for MEF RNA-seq) and GSE156830 (for human HepG2 RNA-seq). Functional clustering in this study was performed using the Database for Annotation, Visualization and Integrated Discovery, version 6.8 (<https://david.ncicrf.gov/home.jsp>). The BXD, LXS and GTEx transcriptome datasets used in this study are available from the GeneNetwork database (<https://www.genenetwork.org>). All data supporting the findings of this study are available from the corresponding author upon request. Source data are provided with this paper.

Received: 9 October 2020; Accepted: 22 December 2020;

Published online: 8 February 2021

References

- Nunnari, J. & Suomalainen, A. Mitochondria: in sickness and in health. *Cell* **148**, 1145–1159 (2012).
- Mottisi, A., Herzig, S. & Auwerx, J. Mitocellular communication: shaping health and disease. *Science* **366**, 827–832 (2019).
- Mishra, P. & Chan, D. C. Mitochondrial dynamics and inheritance during cell division, development and disease. *Nat. Rev. Mol. Cell Biol.* **15**, 634–646 (2014).
- Vafai, S. B. & Mootha, V. K. Mitochondrial disorders as windows into an ancient organelle. *Nature* **491**, 374–383 (2012).
- Sun, N., Youle, R. J. & Finkel, T. The mitochondrial basis of aging. *Mol. Cell* **61**, 654–666 (2016).
- Booth, L. N. & Brunet, A. The aging epigenome. *Mol. Cell* **62**, 728–744 (2016).
- Singh, P. P., Demmitt, B. A., Nath, R. D. & Brunet, A. The genetics of aging: a vertebrate perspective. *Cell* **177**, 200–220 (2019).
- West, A. P., Shadel, G. S. & Ghosh, S. Mitochondria in innate immune responses. *Nat. Rev. Immunol.* **11**, 389–402 (2011).
- West, A. P. & Shadel, G. S. Mitochondrial DNA in innate immune responses and inflammatory pathology. *Nat. Rev. Immunol.* **17**, 363–375 (2017).
- Shpilka, T. & Haynes, C. M. The mitochondrial UPR: mechanisms, physiological functions and implications in ageing. *Nat. Rev. Mol. Cell Biol.* **19**, 109–120 (2018).
- Higuchi-Sanabria, R., Frankino, P. A., Paul, J. W. III, Tronnes, S. U. & Dillin, A. A futile battle? Protein quality control and the stress of aging. *Dev. Cell* **44**, 139–163 (2018).
- Jovaisaite, V. & Auwerx, J. The mitochondrial unfolded protein response—synchronizing genomes. *Curr. Opin. Cell Biol.* **33**, 74–81 (2015).
- Houtkooper, R. H. et al. Mitonuclear protein imbalance as a conserved longevity mechanism. *Nature* **497**, 451–457 (2013).
- Liu, Y., Samuel, B. S., Breen, P. C. & Ruvkun, G. *Caenorhabditis elegans* pathways that surveil and defend mitochondria. *Nature* **508**, 406–410 (2014).
- Pellegrino, M. W. et al. Mitochondrial UPR-regulated innate immunity provides resistance to pathogen infection. *Nature* **516**, 414–417 (2014).
- Zhou, R., Yazdi, A. S., Menu, P. & Tschopp, J. A role for mitochondria in NLRP3 inflammasome activation. *Nature* **469**, 221–225 (2011).
- West, A. P. et al. Mitochondrial DNA stress primes the antiviral innate immune response. *Nature* **520**, 553–557 (2015).
- Nargund, A. M., Pellegrino, M. W., Fiorese, C. J., Baker, B. M. & Haynes, C. M. Mitochondrial import efficiency of ATFS-1 regulates mitochondrial UPR activation. *Science* **337**, 587–590 (2012).
- Quiros, P. M. et al. Multi-omics analysis identifies ATF4 as a key regulator of the mitochondrial stress response in mammals. *J. Cell Biol.* **216**, 2027–2045 (2017).
- Fiorese, C. J. et al. The transcription factor ATF5 mediates a mammalian mitochondrial UPR. *Curr. Biol.* **26**, 2037–2043 (2016).
- Munch, C. & Harper, J. W. Mitochondrial unfolded protein response controls matrix pre-RNA processing and translation. *Nature* **534**, 710–713 (2016).
- Fessler, E. et al. A pathway coordinated by DELE1 relays mitochondrial stress to the cytosol. *Nature* **579**, 433–437 (2020).
- Guo, X. et al. Mitochondrial stress is relayed to the cytosol by an OMA1–DELE1–HRI pathway. *Nature* **579**, 427–432 (2020).
- Tian, Y. et al. Mitochondrial stress induces chromatin reorganization to promote longevity and UPR^m. *Cell* **165**, 1197–1208 (2016).
- Merkwirth, C. et al. Two conserved histone demethylases regulate mitochondrial stress-induced longevity. *Cell* **165**, 1209–1223 (2016).
- Schroeder, E. A., Raimundo, N. & Shadel, G. S. Epigenetic silencing mediates mitochondria stress-induced longevity. *Cell Metab.* **17**, 954–964 (2013).
- Yoneda, T. et al. Compartment-specific perturbation of protein handling activates genes encoding mitochondrial chaperones. *J. Cell Sci.* **117**, 4055–4066 (2004).
- Durieux, J., Wolff, S. & Dillin, A. The cell-non-autonomous nature of electron transport chain-mediated longevity. *Cell* **144**, 79–91 (2011).
- Verdin, E. & Ott, M. 50 years of protein acetylation: from gene regulation to epigenetics, metabolism and beyond. *Nat. Rev. Mol. Cell Biol.* **16**, 258–264 (2015).
- Menzies, K. J., Zhang, H. B., Katsyuba, E. & Auwerx, J. Protein acetylation in metabolism—metabolites and cofactors. *Nat. Rev. Endocrinol.* **12**, 43–60 (2016).
- Lee, K. K. & Workman, J. L. Histone acetyltransferase complexes: one size doesn't fit all. *Nat. Rev. Mol. Cell Biol.* **8**, 284–295 (2007).
- Sheikh, B. N. & Akhtar, A. The many lives of KATs—detectors, integrators and modulators of the cellular environment. *Nat. Rev. Genet.* **20**, 7–23 (2019).
- Shi, Y. & Mello, C. A CBP/p300 homolog specifies multiple differentiation pathways in *Caenorhabditis elegans*. *Genes Dev.* **12**, 943–955 (1998).
- Chrivia, J. C. et al. Phosphorylated CREB binds specifically to the nuclear protein CBP. *Nature* **365**, 855–859 (1993).
- Arany, Z., Sellers, W. R., Livingston, D. M. & Eckner, R. E1A-associated p300 and CREB-associated CBP belong to a conserved family of coactivators. *Cell* **77**, 799–800 (1994).
- Kasper, L. H. et al. CBP/p300 double null cells reveal effect of coactivator level and diversity on CREB transactivation. *EMBO J.* **29**, 3660–3672 (2010).
- Weinert, B. T. et al. Time-resolved analysis reveals rapid dynamics and broad scope of the CBP/p300 acetylome. *Cell* **174**, 231–244.e12 (2018).
- Lasko, L. M. et al. Discovery of a selective catalytic p300/CBP inhibitor that targets lineage-specific tumours. *Nature* **550**, 128–132 (2017).
- Chekler, E. L. et al. Transcriptional profiling of a selective CREB binding protein bromodomain inhibitor highlights therapeutic opportunities. *Chem. Biol.* **22**, 1588–1596 (2015).
- Nolden, M. et al. The m-AAA protease defective in hereditary spastic paraplegia controls ribosome assembly in mitochondria. *Cell* **123**, 277–289 (2005).
- Kim, H. E. et al. Lipid biosynthesis coordinates a mitochondrial-to-cytosolic stress response. *Cell* **166**, 1539–1552 (2016).
- Lin, Y. F. & Haynes, C. M. Metabolism and the UPR^m. *Mol. Cell* **61**, 677–682 (2016).
- Wu, Y. et al. Multilayered genetic and omics dissection of mitochondrial activity in a mouse reference population. *Cell* **158**, 1415–1430 (2014).
- Marmorstein, R. & Zhou, M. M. Writers and readers of histone acetylation: structure, mechanism, and inhibition. *Cold Spring Harb. Perspect. Biol.* **6**, a018762 (2014).
- Rauthan, M., Ranji, P., Pradenas, N. A., Pitot, C. & Pilon, M. The mitochondrial unfolded protein response activator ATFS-1 protects cells from inhibition of the mevalonate pathway. *Proc. Natl Acad. Sci. USA* **110**, 5981–5986 (2013).
- Lakowski, B. & Hekimi, S. Determination of life-span in *Caenorhabditis elegans* by four clock genes. *Science* **272**, 1010–1013 (1996).
- Feng, J., Bussiere, F. & Hekimi, S. Mitochondrial electron transport is a key determinant of life span in *Caenorhabditis elegans*. *Dev. Cell* **1**, 633–644 (2001).
- Dillin, A. et al. Rates of behavior and aging specified by mitochondrial function during development. *Science* **298**, 2398–2401 (2002).
- Zhang, M. et al. Role of CBP and SATB-1 in aging, dietary restriction, and insulin-like signaling. *PLoS Biol.* **7**, e1000245 (2009).
- Sorrentino, V. et al. Enhancing mitochondrial proteostasis reduces amyloid- β proteotoxicity. *Nature* **552**, 187–193 (2017).
- McColl, G. et al. Utility of an improved model of amyloid-beta ($A\beta_{1-42}$) toxicity in *Caenorhabditis elegans* for drug screening for Alzheimer's disease. *Mol. Neurodegener.* <https://doi.org/10.1186/1750-1326-7-57> (2012).
- Andreux, P. A. et al. Systems genetics of metabolism: the use of the BXD murine reference panel for multiscalar integration of traits. *Cell* **150**, 1287–1299 (2012).

53. Williams, R. W. et al. Genetic structure of the LXS panel of recombinant inbred mouse strains: a powerful resource for complex trait analysis. *Mamm. Genome* **15**, 637–647 (2004).
54. Consortium, G. T. Human genomics. The Genotype-Tissue Expression (GTEx) pilot analysis: multitissue gene regulation in humans. *Science* **348**, 648–660 (2015).
55. Molenaars, M. et al. A conserved mito-cytosolic translational balance links two longevity pathways. *Cell Metab.* **31**, 549–563 (2020).
56. Bao, X. R. et al. Mitochondrial dysfunction remodels one-carbon metabolism in human cells. *eLife* <https://doi.org/10.7554/eLife.10575> (2016).
57. Schueller, E. et al. Dysregulation of histone acetylation pathways in hippocampus and frontal cortex of Alzheimer's disease patients. *Eur. Neuropsychopharm.* **33**, 101–116 (2020).
58. Nucifora, F. C. et al. Interference by huntingtin and atrophin-1 with CBP-mediated transcription leading to cellular toxicity. *Science* **291**, 2423–2428 (2001).
59. Nativio, R. et al. An integrated multi-omics approach identifies epigenetic alterations associated with Alzheimer's disease. *Nat. Genet.* **52**, 1024–1035 (2020).
60. Caccamo, A., Maldonado, M. A., Bokov, A. F., Majumder, S. & Oddo, S. CBP gene transfer increases BDNF levels and ameliorates learning and memory deficits in a mouse model of Alzheimer's disease. *Proc. Natl Acad. Sci. USA* **107**, 22687–22692 (2010).
61. Chatterjee, S. et al. Reinstating plasticity and memory in a tauopathy mouse model with an acetyltransferase activator. *EMBO Mol. Med.* <https://doi.org/10.15252/emmm.201708587> (2018).
62. Cutler, T. et al. *Drosophila* eye model to study neuroprotective role of CREB binding protein (CBP) in Alzheimer's disease. *PLoS ONE* <https://doi.org/10.1371/journal.pone.0137691> (2015).
63. Wellen, K. E. et al. ATP-citrate lyase links cellular metabolism to histone acetylation. *Science* **324**, 1076–1080 (2009).
64. Canto, C. et al. AMPK regulates energy expenditure by modulating NAD⁺ metabolism and SIRT1 activity. *Nature* **458**, 1056–1060 (2009).
65. Rodgers, J. T. et al. Nutrient control of glucose homeostasis through a complex of PGC-1 α and SIRT1. *Nature* **434**, 113–118 (2005).
66. Lassot, I. et al. p300 modulates ATF4 stability and transcriptional activity independently of its acetyltransferase domain. *J. Biol. Chem.* **280**, 41537–41545 (2005).
67. Yin, J. A. et al. Genetic variation in glia–neuron signalling modulates ageing rate. *Nature* **551**, 198–203 (2017).
68. Magnoni, R. et al. Late onset motoneuron disorder caused by mitochondrial Hsp60 chaperone deficiency in mice. *Neurobiol. Dis.* **54**, 12–23 (2013).
69. Kurdستاني, S. K., Tavazoie, S. & Grunstein, M. Mapping global histone acetylation patterns to gene expression. *Cell* **117**, 721–733 (2004).
70. Mouchiroud, L. et al. The NAD⁺/sirtuin pathway modulates longevity through activation of mitochondrial UPR and FOXO signaling. *Cell* **154**, 430–441 (2013).
71. Andrews, S. FastQC: a quality control tool for high throughput sequence data. <http://www.bioinformatics.babraham.ac.uk/projects/fastqc> (2010).
72. Dobin, A. et al. STAR: ultrafast universal RNA-seq aligner. *Bioinformatics* **29**, 15–21 (2013).
73. Anders, S., Pyl, P. T. & Huber, W. HTSeq—a Python framework to work with high-throughput sequencing data. *Bioinformatics* **31**, 166–169 (2015).
74. Law, C. W., Chen, Y., Shi, W. & Smyth, G. K. voom: precision weights unlock linear model analysis tools for RNA-seq read counts. *Genome Biol.* **15**, R29 (2014).
75. Ritchie, M. E. et al. limma powers differential expression analyses for RNA-sequencing and microarray studies. *Nucleic Acids Res.* **43**, e47 (2015).
76. Huang, D. W., Sherman, B. T. & Lempicki, R. A. Systematic and integrative analysis of large gene lists using DAVID bioinformatics resources. *Nat. Protoc.* **4**, 44–57 (2009).
77. Mukhopadhyay, A., Deplancke, B., Walhout, A. J. & Tissenbaum, H. A. Chromatin immunoprecipitation (ChIP) coupled to detection by quantitative real-time PCR to study transcription factor binding to DNA in *Caenorhabditis elegans*. *Nat. Protoc.* **3**, 698–709 (2008).
78. Langmead, B. & Salzberg, S. L. Fast gapped-read alignment with Bowtie 2. *Nat. Methods* **9**, 357–359 (2012).
79. Li, H. et al. The sequence Alignment/Map format and SAMtools. *Bioinformatics* **25**, 2078–2079 (2009).
80. Zhang, Y. et al. Model-based analysis of ChIP-Seq (MACS). *Genome Biol.* **9**, R137 (2008).
81. Carroll, T. S., Liang, Z., Salama, R., Stark, R. & de Santiago, I. Impact of artifact removal on ChIP quality metrics in ChIP-seq and ChIP-exo data. *Front. Genet.* **5**, 75 (2014).
82. Quinlan, A. R. & Hall, I. M. BEDTools: a flexible suite of utilities for comparing genomic features. *Bioinformatics* **26**, 841–842 (2010).
83. Wang, M., Zhao, Y. & Zhang, B. Efficient test and visualization of multi-set intersections. *Sci. Rep.* **5**, 16923 (2015).
84. Robinson, J. T. et al. Integrative genomics viewer. *Nat. Biotechnol.* **29**, 24–26 (2011).
85. Kirienko, N. V., Cezairliyan, B. O., Ausubel, F. M. & Powell, J. R. *Pseudomonas aeruginosa* PA14 pathogenesis in *Caenorhabditis elegans*. *Methods Mol. Biol.* **1149**, 653–669 (2014).
86. Askew, E. B., Bai, S., Blackwelder, A. J. & Wilson, E. M. Transcriptional synergy between melanoma antigen gene protein-A11 (MAGE-11) and p300 in androgen receptor signaling. *J. Biol. Chem.* **285**, 21824–21836 (2010).
87. Krzywinski, M. et al. Circos: an information aesthetic for comparative genomics. *Genome Res.* **19**, 1639–1645 (2009).

Acknowledgements

We thank the *Caenorhabditis* Genetics Center for providing the *C. elegans* strains. We thank P. K. Brindle for providing the *CBP/p300*^{-/-} MEFs. We thank all members of the J. Auwerx and K. Schoonjans laboratories for helpful discussions. This work was supported by grants from the École Polytechnique Fédérale de Lausanne, European Research Council (ERC-AdG-787702) and Swiss National Science Foundation (31003A_179435) and a Global Research Laboratory grant from the National Research Foundation of Korea (2017K1A1A2013124). T.Y.L. was supported by the Human Frontier Science Program (LT000731/2018-L). L.J.E.G. is supported by a Swiss Government Excellence Scholarship (FCS ESKAS-Nr. 2019.0009).

Author contributions

T.Y.L. and J.A. conceived of the project. T.Y.L. performed most of the experiments. A.W.G. contributed to the *C. elegans* lifespan experiments. A.M. contributed to the *P. aeruginosa* infection experiment. T.Y.L., M.B.S., H.L., A.M.B., G.E.A., X.L. and L.J.E.G. performed the data analysis. K.S. and J.A. supervised the study. T.Y.L. and J.A. wrote the manuscript with comments from all authors.

Competing interests

The authors declare no competing interests.

Additional information

Supplementary information The online version contains supplementary material available at <https://doi.org/10.1038/s43587-020-00025-z>.

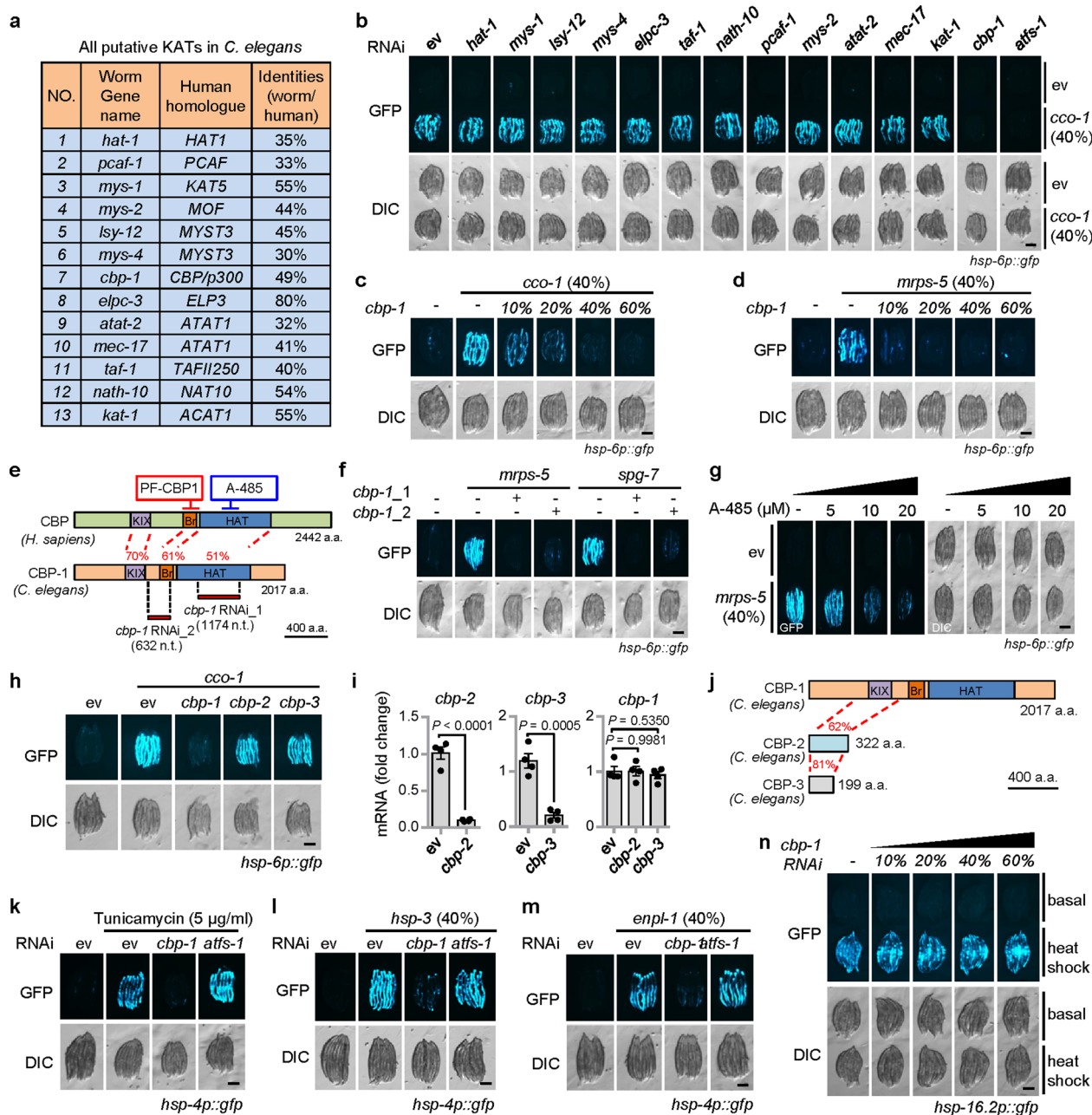
Correspondence and requests for materials should be addressed to J.A.

Peer review information *Nature Aging* thanks the anonymous reviewers for their contribution to the peer review of this work.

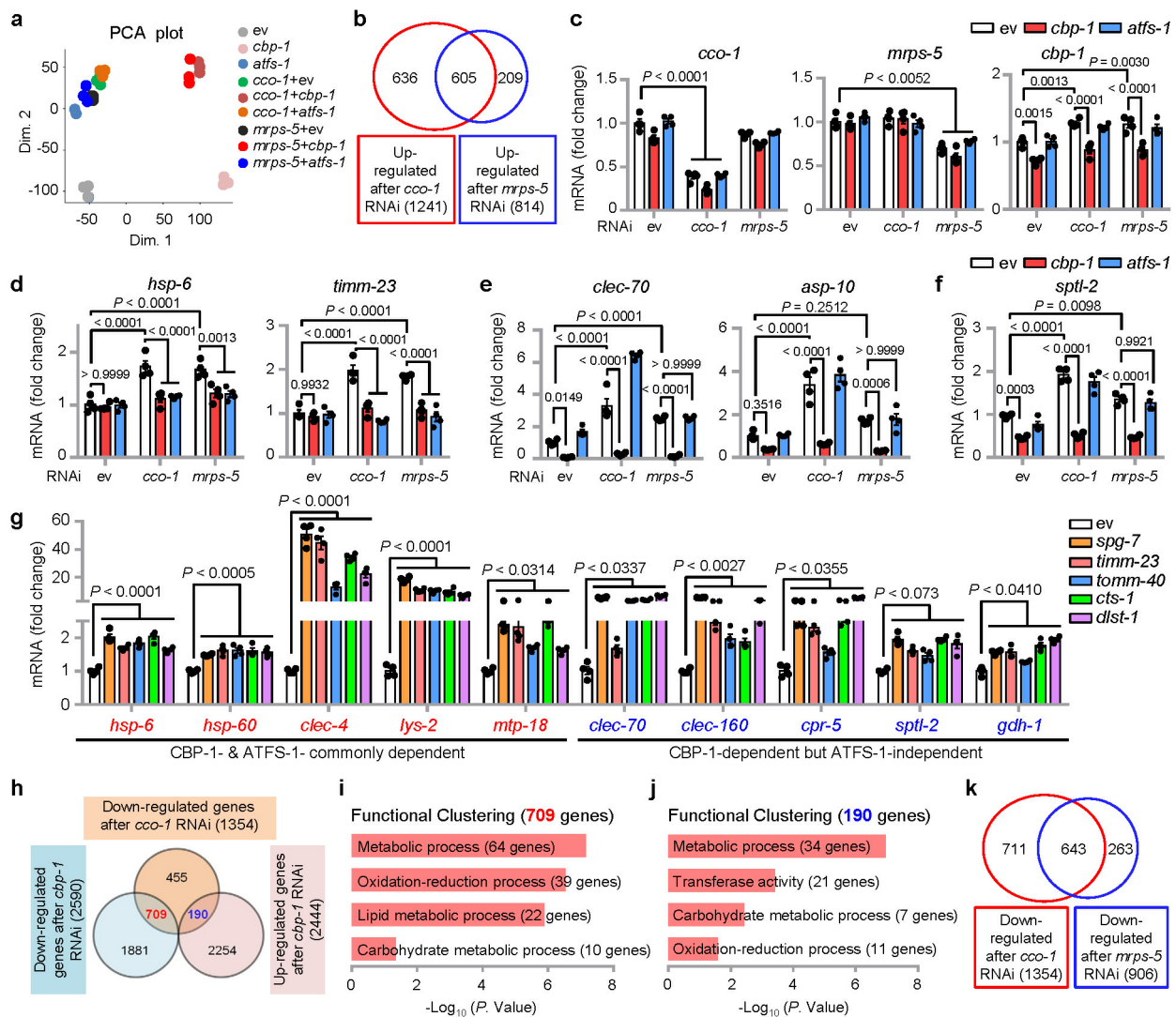
Reprints and permissions information is available at www.nature.com/reprints.

Publisher's note Springer Nature remains neutral with regard to jurisdictional claims in published maps and institutional affiliations.

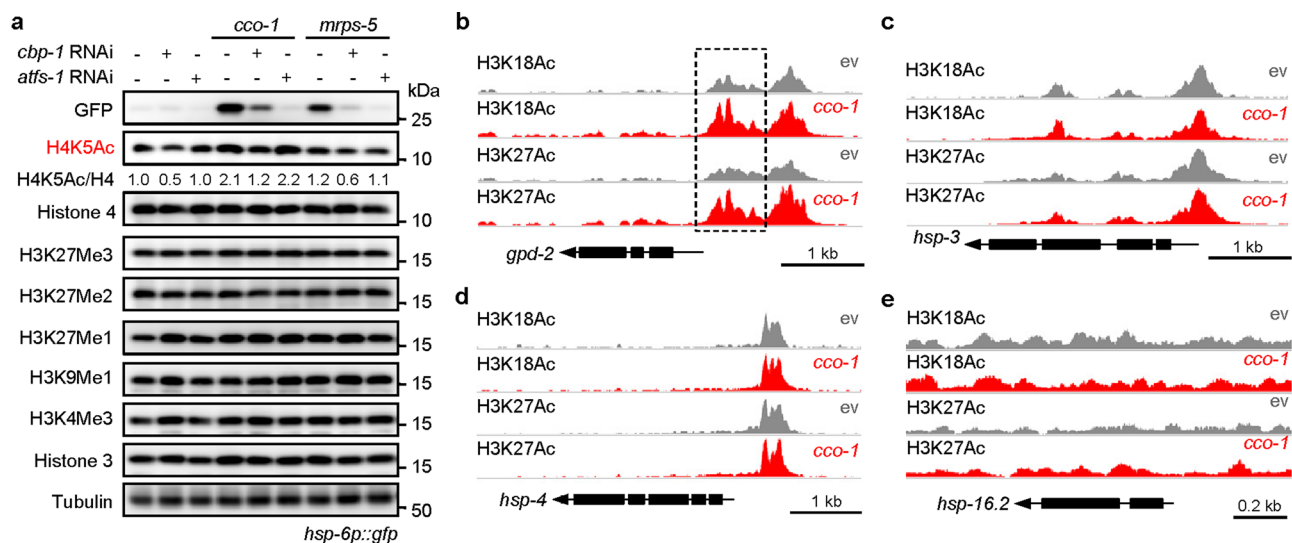
© The Author(s), under exclusive licence to Springer Nature America, Inc. 2021



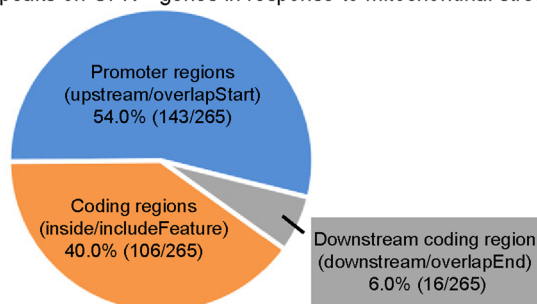
Extended Data Fig. 1 | Inhibition of CBP-1 by RNAi or pharmacological inhibitors attenuates UPR^{mt} activation in *C. elegans*. **a**, All putative lysine acetyltransferases (KATs) in *C. elegans* and their human homologues. The worm KATs were validated/identified by searching the *C. elegans* protein database for proteins with a conserved acetyltransferase domain, and high amino acid sequences identities of the known human KATs³⁰. **b**, Role of KATs in UPR^{mt} activation in *C. elegans*. *hsp-6p::gfp* worms were fed with control (ev) or *cco-1* (40%) RNAi in combination with RNAi targeting different KATs (60%). **c**, **d**, *cbp-1* RNAi attenuates the UPR^{mt} activation induced by *cco-1* (c) or *mrps-5* (d) RNAi in a dose-dependent manner. RNAi targeting *cco-1* or *mrps-5* occupied 40%. *cbp-1* RNAi occupied 10-60%. Control RNAi was used to supply to a final 100% of RNAi for all conditions. **e**, Schematic diagram showing the different regions regulated by the two different *cbp-1* RNAi, and the two CBP/p300 inhibitors (PF-CBP1 and A-485). KIX, kinase-inducible domain interacting domain; Br, bromodomain; HAT, histone acetyltransferase domain; a.a., amino acids; n.t., nucleotides. **f**, The alternative *cbp-1* RNAi (*cbp-1_2*) also inhibits UPR^{mt} activation. RNAi targeting *mrps-5* or *spg-7* occupies 40%, *cbp-1* RNAi occupies 25%. **g**, A-485 attenuates UPR^{mt} activation induced by *mrps-5* RNAi in a dose-dependent manner. *hsp-6p::gfp* worms were fed with control or *mrps-5* RNAi (40%), in combination with 0-20 μM A-485. **h**, **i**, RNAi that specifically targets *cbp-2* or *cbp-3* failed to abolish UPR^{mt} activation in *hsp-6p::gfp* worms. Photos (h) and qRT-PCR-results (*n* = 4 biologically independent samples) (i) of *hsp-6p::gfp* worms fed with control, *cco-1* (40%), *cbp-1* (25%), *cbp-2* (Ahringer library) or *cbp-3* RNAi. Error bars denote SEM. Statistical analysis was performed by two-tailed unpaired Student's *t*-test. **j**, Schematic diagram showing the protein structure of CBP-1, CBP-2 and CBP-3. The numbers in red indicate the amino acid sequence identities between two proteins in comparison. **k-m**, *cbp-1* RNAi attenuates the UPR^{ER} activation induced by tunicamycin (5 μg/ml) (k), *hsp-3* (l) or *enpl-1* (m) RNAi in *hsp-4p::gfp* worms. RNAi targeting *hsp-3* or *enpl-1* occupies 40%, *cbp-1* RNAi occupies 25%, *atfs-1* RNAi occupies 60%. **n**, *cbp-1* RNAi does not affect the cytosolic UPR (UPR^{CYT})/heat shock response activation induced by heat shock. *hsp16.2p::gfp* reporter worms were fed with different percentages of *cbp-1* RNAi as indicated. As positive control, heat shock for 8 h at 31 °C could induce the UPR^{CYT} and *cbp-1* RNAi did not block this response. Scale bars, 0.3 mm.



Extended Data Fig. 2 | UPR^{mt} genes dependent or independent of CBP-1 and ATFS-1 for expression. **a**, Principal-component analysis (PCA) of the RNA-seq profiles of worms treated with the indicated RNAi. **b**, Diagram of genes up-regulated after *cco-1* RNAi, in common with genes up-regulated after *mrps-5* RNAi according to the RNA-seq data. **c-f**, qRT-PCR-results of indicated genes in *hsp-6p::gfp* worms fed with control (ev), *cco-1*, *mrps-5*, *cbp-1* or *atfs-1* RNAi ($n = 4$ biologically independent samples). RNAi targeting *cco-1* or *mrps-5* occupies 50%, *cbp-1* occupies 25%, *atfs-1* occupies 50%. **g**, qRT-PCR-results of *hsp-6p::gfp* worms fed with control (ev), *spg-7*, *timmm-23*, *tomm-40*, *cts-1* or *dst-1* RNAi ($n = 4$ biologically independent samples). UPR^{mt} genes dependent on both CBP-1 and ATFS-1 for induction according to the RNA-seq dataset (as summarized in Fig. 1g) are highlighted in red. Genes only dependent on CBP-1, but not ATFS-1, are highlighted in blue. **h**, Diagram of the down-regulated genes after single *cco-1* RNAi (orange), in common with down-regulated (blue) or up-regulated (pink) genes after single *cbp-1* RNAi according to the RNA-seq data. **i, j**, Functional clustering of the 709 (i) and 190 (j) genes as indicated in (h). **k**, Diagram of genes down-regulated after *cco-1* RNAi, in common with genes down-regulated after *mrps-5* RNAi according to the RNA-seq data. Error bars denote SEM. Statistical analysis was performed by ANOVA followed by Tukey post-hoc test.

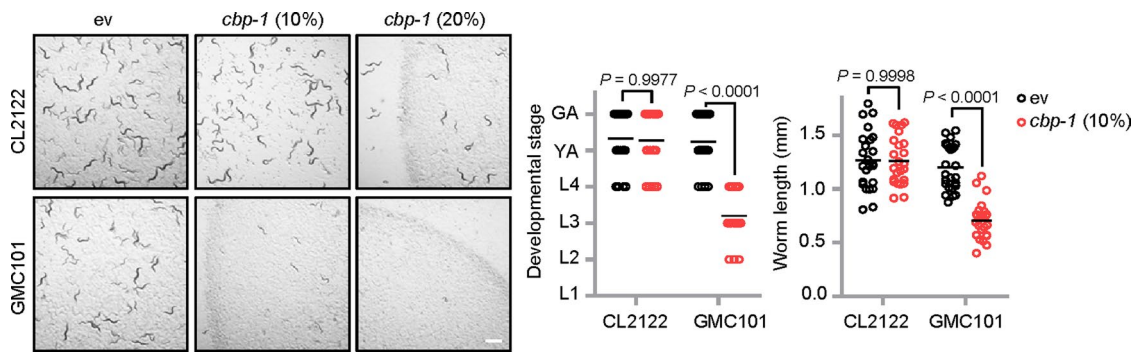


f Distribution analysis of the 265 increased H3K18Ac/H3K27Ac peaks on UPR^{mt} genes in response to mitochondrial stress

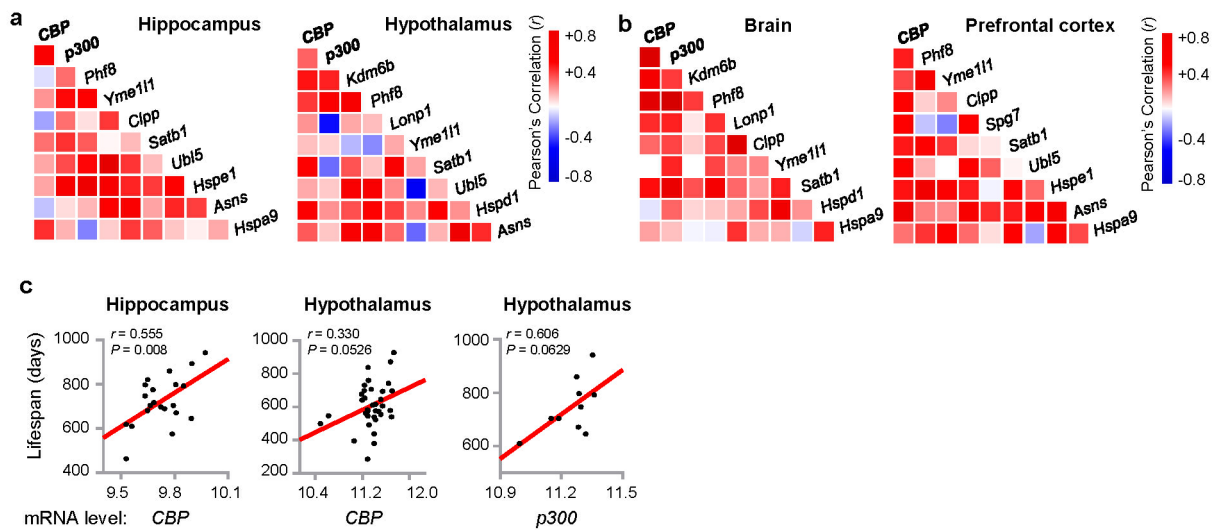


Extended Data Fig. 3 | Mitochondrial stress increases CBP-1-mediated histone acetylation at the loci of UPR^{mt}, but not UPR^{ER} or UPR^{CYT} genes.

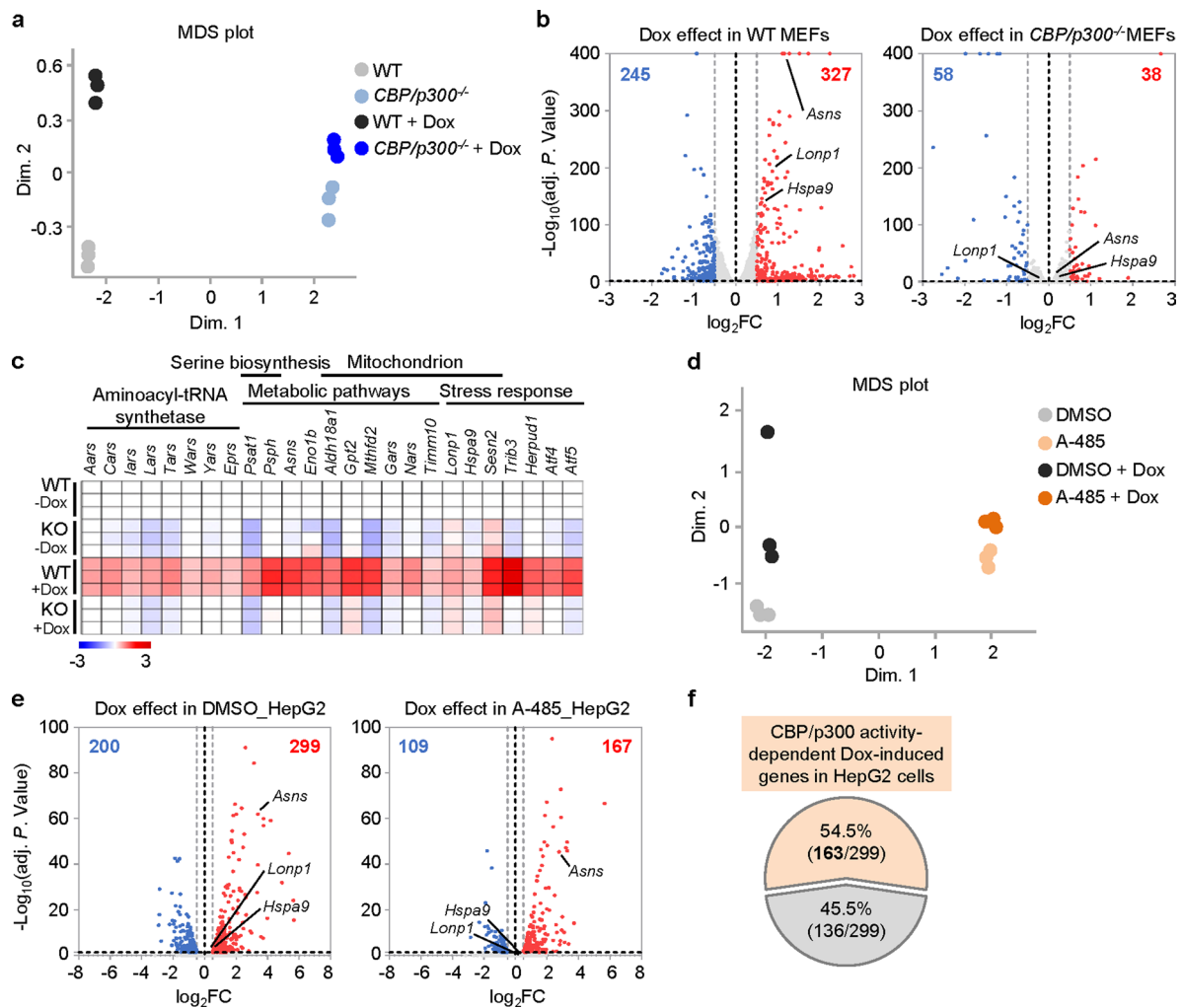
a, Western blots of *hsp-6p::gfp* worms fed with control, *cbp-1*, *atfs-1*, *cco-1* or *mrps-5* RNAi. RNAi targeting *cbp-1* occupies 25%, *atfs-1*, *cco-1* or *mrps-5* occupies 50%. **b-e**, Genome tracks showing the ChIP-seq analysis for H3K27Ac and H3K18Ac over the genomic loci of *gpd-2* (b), *hsp-3* (c), *hsp-4* (d) and *hsp-16.2* (e) in worms fed with control or *cco-1* RNAi. The two tracks were shown with the same total count range between basal and mitochondrial stress condition for each gene. **f**, Summary of the distribution analysis of the 265 increased H3K18Ac/H3K27Ac peaks on the 134 UPR^{mt} genes (as indicated in Fig. 2d) in response to mitochondrial stress. For uncropped gel source data, see Source Extended Data Fig. 3.



Extended Data Fig. 4 | RNAi of *cbp-1* caused a severe developmental delay in the worm Alzheimer's disease model GMC101, but not in the control CL2122 strain. Representative photos of CL2122 or GMC101 worms fed with control or *cbp-1* (10% or 20%) RNAi since maternal L4 stage. The developmental stage and body length of the F1 progeny were quantified at Day 4 after hatching ($n = 25$ worms for each condition). Conditions with 20% *cbp-1* RNAi were not quantified as most of the eggs failed to hatch in GMC101 worms fed with 20% *cbp-1* RNAi. Scale bar, 1mm. Error bars denote SEM. Statistical analysis was performed by ANOVA followed by Tukey post-hoc test.



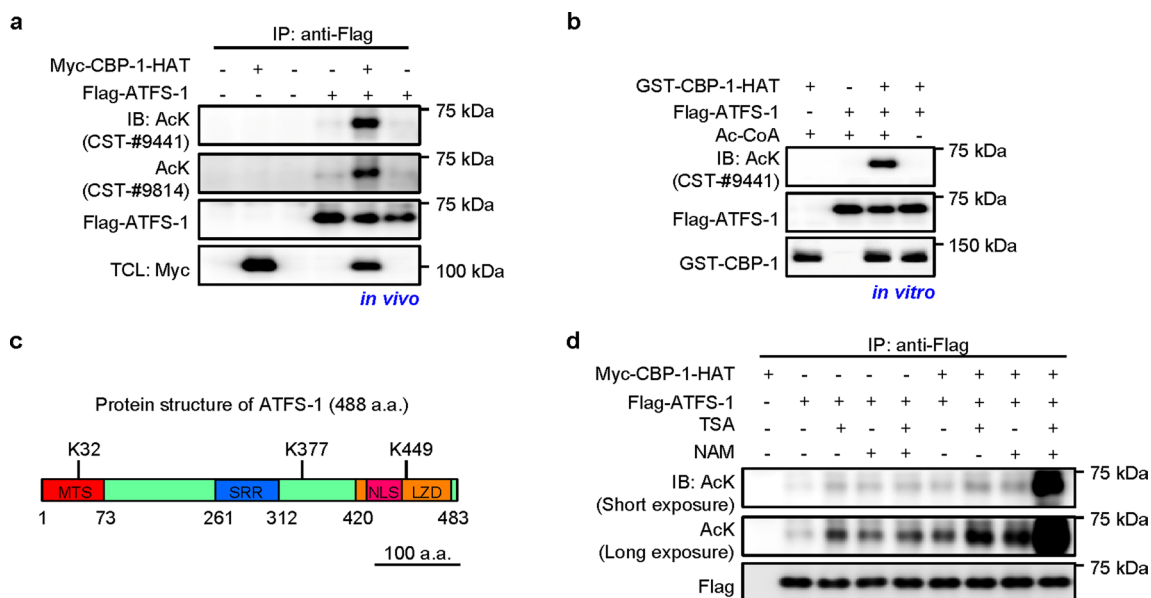
Extended Data Fig. 5 | *CBP*/*p300* expression positively correlates with *Kdm6b*/*Phf8*, UPR^{mt} transcripts and lifespan in mouse populations. **a**, Pearson's correlation co-expression heat-map for *CBP*/*p300*, *Kdm6b*/*Phf8* and UPR^{mt} genes in hippocampus and hypothalamus of the BXD mouse genetic reference population^{43,52}. Positive and negative correlations are indicated in red and blue, respectively. The intensity of the colors corresponds to correlation coefficients. **b**, Pearson's correlation co-expression heat-map for *CBP*/*p300*, *Kdm6b*/*Phf8* and UPR^{mt} genes in the brain (whole brain) and prefrontal cortex of the LXS mouse genetic reference population⁵³. **c**, Positive correlations between lifespan and *CBP* or *p300* transcript levels in hippocampus and hypothalamus of BXD mice (Pearson's r , two-sided). Each dot indicates an independent BXD strain.



Extended Data Fig. 6 | An essential role of CBP/p300 and CBP/p300 acetyltransferase activity in UPR^{mt} activation in mammalian cells.

a, Multidimensional scaling (MDS) plot of the RNA-seq profiles of wild-type (WT) and *CBP/p300*^{-/-} MEFs treated with or without Dox (30 μg/ml) for 24 h. Note the decreased distance between Dox-treated and un-treated condition in the *CBP/p300*^{-/-} background compared to that in WT background.

b, *CBP/p300*^{-/-} MEFs are insensitive to the treatment of mitochondrial stress inducer Dox. Volcano plots showing the effect of Dox treatment in wild-type (WT) (left) or *CBP/p300*^{-/-} (right) MEFs on gene expression. FC, fold change. Genes that were up-regulated ($\log_2FC > 0.5$, adjusted $P < 0.05$) during Dox treatment were highlighted in red. Genes that were down-regulated ($\log_2FC < -0.5$, adjusted $P < 0.05$) were highlighted in blue. **c**, Heat-map of the representative UPR^{mt} genes dependent on CBP/p300 for induction in response to Dox treatment in WT and *CBP/p300*^{-/-} (KO) MEFs, according to the RNA-seq data. The heat-map was shown in \log_2FC values. **d**, MDS plot of the RNA-seq profiles of HepG2 cells treated with or without CBP/p300 acetyltransferase activity inhibitor A-485 (5 μM) and/or Dox (30 μg/ml) for 24 h. **e**, The CBP/p300 catalytic inhibitor A-485 attenuates the effect of Dox on gene expression in HepG2 cells. Volcano plots showing the effect of Dox on gene expression of HepG2 cells in control (DMSO) (left) or A-485 (right) treatment background. FC, fold change. Genes that were up-regulated ($\log_2FC > 0.5$, adjusted $P < 0.05$) during Dox treatment were highlighted in red. Genes that were down-regulated ($\log_2FC < -0.5$, adjusted $P < 0.05$) were highlighted in blue. **f**, Diagram of the UPR^{mt} genes that are dependent (orange) or independent (grey) on CBP/p300 activity in response to Dox treatment in HepG2 cells, according to the RNA-seq data with A-485.



Extended Data Fig. 7 | ATFS-1 can be acetylated by CBP-1 and affected by both class I/II and class III HDACs. **a**, ATFS-1 was acetylated by CBP-1 *in vivo*. Flag-tagged ATFS-1 was expressed with or without CBP-1 acetyltransferase domain (CBP-1-HAT) in HEK293T cells, immunoprecipitated with anti-Flag antibody and analyzed by western blots. TCL, total cell lysate. **b**, ATFS-1 was acetylated by CBP-1 *in vitro*. Bacterially expressed GST tagged CBP-1-HAT was incubated with Flag-ATFS-1 with or without acetyl-CoA (Ac-CoA) and immunoblotted as indicated. **c**, Schematic diagram showing the protein structure of ATFS-1 and the acetylated sites identified by mass spectrometry. MTS, mitochondrial targeting sequence; SRR, Serine-rich region; NLS, Nuclear localization signal; LZD, Leucine zipper domain. **d**, HEK293T cells transfected as indicated were treated with or without TSA (class I/II HDAC inhibitor), or NAM (class III HDAC inhibitor) 8 h before harvesting, and analyzed by western blots. For uncropped gel source data, see Source Extended Data Fig. 7.

Reporting Summary

Nature Research wishes to improve the reproducibility of the work that we publish. This form provides structure for consistency and transparency in reporting. For further information on Nature Research policies, see our [Editorial Policies](#) and the [Editorial Policy Checklist](#).

Statistics

For all statistical analyses, confirm that the following items are present in the figure legend, table legend, main text, or Methods section.

n/a Confirmed

- The exact sample size (n) for each experimental group/condition, given as a discrete number and unit of measurement
- A statement on whether measurements were taken from distinct samples or whether the same sample was measured repeatedly
- The statistical test(s) used AND whether they are one- or two-sided
Only common tests should be described solely by name; describe more complex techniques in the Methods section.
- A description of all covariates tested
- A description of any assumptions or corrections, such as tests of normality and adjustment for multiple comparisons
- A full description of the statistical parameters including central tendency (e.g. means) or other basic estimates (e.g. regression coefficient) AND variation (e.g. standard deviation) or associated estimates of uncertainty (e.g. confidence intervals)
- For null hypothesis testing, the test statistic (e.g. F , t , r) with confidence intervals, effect sizes, degrees of freedom and P value noted
Give P values as exact values whenever suitable.
- For Bayesian analysis, information on the choice of priors and Markov chain Monte Carlo settings
- For hierarchical and complex designs, identification of the appropriate level for tests and full reporting of outcomes
- Estimates of effect sizes (e.g. Cohen's d , Pearson's r), indicating how they were calculated

Our web collection on [statistics for biologists](#) contains articles on many of the points above.

Software and code

Policy information about [availability of computer code](#)

Data collection

Microscopy pictures were acquired with Zeiss LSM 700 Upright confocal microscope (Carl Zeiss AG); Victor X4 plate reader (Perkin Elmer) was used for all the assays requiring absorbance, luminescence or fluorescence quantifications; oxygen consumption was measured with the Seahorse XF96 instrument (Seahorse Bioscience); the qPCR reactions were performed using the Light-Cycler system (Roche Applied Science).

RNA-seq analysis was performed using the R version 3.6.3, FastQC was used to verify the quality of the sequence data. Sequenced reads were mapped using STAR aligner version 2.6.0a. Reads were counted using htseq-count version 0.10.0. Differential expression of genes was calculated by using Limma-Voom.

ChIP-seq analysis was performed using the R version 3.6.3, FastQC was used to verify the quality of the sequence data. alignment was performed by using Bowtie2 (version 2.3.5). SAMtools (version 1.4.1) was used to sort, filter and index the obtained alignments. Peak calling was then performed using MACS2 (version 2.1.2). Quality of alignment and peaks were assessed using the ChIPQC (version 1.18.2). Read counts per peak were obtained using BEDTools (version 2.26.0) and SAMtools (version 1.4.1). Intersection between sets and their associated p-values were computed using the SuperExactTest7 (version 1.0.6) package.

Data analysis

GraphPad Prism 6 for Mac OS X (GraphPad Software, Inc.). Fiji (<http://imagej.nih.gov/ij/>; version 1.47b). Heat-maps were generated by using Morpheus (<https://software.broadinstitute.org/morpheus>). The Circos plot was generated using Circos (<http://www.circos.ca>). Genome tracks were revealed by Integrative Genomics Viewer IGV (version 2.8.0).

For manuscripts utilizing custom algorithms or software that are central to the research but not yet described in published literature, software must be made available to editors and reviewers. We strongly encourage code deposition in a community repository (e.g. GitHub). See the Nature Research [guidelines for submitting code & software](#) for further information.

Data

Policy information about [availability of data](#)

All manuscripts must include a [data availability statement](#). This statement should provide the following information, where applicable:

- Accession codes, unique identifiers, or web links for publicly available datasets
- A list of figures that have associated raw data
- A description of any restrictions on data availability

The RNA/DNA sequencing datasets have been deposited in the NCBI Gene Expression Omnibus (GEO) database (<https://www.ncbi.nlm.nih.gov/geo/>) with the accession numbers: GSE131611 for worm RNA-seq, GSE148328 for worm ChIP-seq, GSE131613 for MEFs RNA-seq and GSE156830 for human HepG2 RNA-seq. Functional clustering in this study was performed by using the DAVID (Database for Annotation, Visualization and Integrated Discovery) database v6.8 (<https://david.ncifcrf.gov/home.jsp>). The BXD, LXS and GTEX transcriptome datasets used in this study are available in the GeneNetwork database (<https://www.genenetwork.org>). All data supporting the findings of this study are available from the corresponding author J.A. upon request. Source data are provided with this paper.

Field-specific reporting

Please select the one below that is the best fit for your research. If you are not sure, read the appropriate sections before making your selection.

- Life sciences Behavioural & social sciences Ecological, evolutionary & environmental sciences

For a reference copy of the document with all sections, see nature.com/documents/nr-reporting-summary-flat.pdf

Life sciences study design

All studies must disclose on these points even when the disclosure is negative.

Sample size	No statistical methods were used to pre-determine sample sizes, but our sample sizes are similar to those reported in previous publications (Houtkooper, R. H. et al. Nature, 2013; Mouchiroud, L. et al. Cell, 2013; Sorrentino, V. et al., Nature, 2017)
Data exclusions	No data were excluded from the analysis, except for the C. elegans lifespan or survival experiments (the reasons for censoring were the “exploded vulva” phenotype or worms that crawled off the plate). These reasons were pre-established before the beginning of the experiment (Houtkooper, R. H. et al. Nature, 2013; Mouchiroud, L. et al. Cell, 2013).
Replication	All the experiments were repeated at least twice and the findings were reliably reproduced
Randomization	For all experiments, samples/C. elegans/cells were allocated to groups/treatments randomly, steps were taken to avoid batch effects
Blinding	The investigators were not blinded to group allocations due to the fact that the genotypes/phenotypes of worms, the effects of RNAi as well as compound treatments, needed to be carefully documented by the investigators during experimental steps, so blinding was not always possible. When possible, data analysis was performed in a blind manner until the group-to-group comparison steps are reached, including the analysis of RNA-seq and ChIP-seq results

Reporting for specific materials, systems and methods

We require information from authors about some types of materials, experimental systems and methods used in many studies. Here, indicate whether each material, system or method listed is relevant to your study. If you are not sure if a list item applies to your research, read the appropriate section before selecting a response.

Materials & experimental systems

n/a	Involved in the study
<input type="checkbox"/>	<input checked="" type="checkbox"/> Antibodies
<input type="checkbox"/>	<input checked="" type="checkbox"/> Eukaryotic cell lines
<input checked="" type="checkbox"/>	<input type="checkbox"/> Palaeontology and archaeology
<input type="checkbox"/>	<input checked="" type="checkbox"/> Animals and other organisms
<input checked="" type="checkbox"/>	<input type="checkbox"/> Human research participants
<input checked="" type="checkbox"/>	<input type="checkbox"/> Clinical data
<input checked="" type="checkbox"/>	<input type="checkbox"/> Dual use research of concern

Methods

n/a	Involved in the study
<input type="checkbox"/>	<input checked="" type="checkbox"/> ChIP-seq
<input checked="" type="checkbox"/>	<input type="checkbox"/> Flow cytometry
<input checked="" type="checkbox"/>	<input type="checkbox"/> MRI-based neuroimaging

Antibodies

Antibodies used

Antibodies against GFP (1:1000, Cat. 2956, CST), Actin (1:2000, Cat. A5441, Sigma), H3K18Ac (1:1000, Cat. 07-354, Merck), H3K27Ac (1:1000, Cat. ab4729, abcam), H3K9Ac (1:1000, Cat. 06-942, Merck), H3K4Ac (1:1000, Cat. Ab176799, abcam), Histone 3 (1:1000, Cat. 9715, CST), Tubulin (1:2000, Cat. T5168, Sigma), H3K27Me3 (1:1000, Cat. 07-449, millipore), H3K27Me2 (1:1000, Cat. ab24684,

Validation

abcam), H3K27Me1 (1:1000, Cat. 07-448, millipore), H3K9Me1 (1:1000, Cat. 07-450, millipore), H3K4Me3 (1:1000, Cat. 07-473, millipore), Histone 4 (1:1000, Cat. sc-10810, Santa Cruz), H4K5Ac (1:1000, Cat. ab51997, abcam), β -amyloid 1–16 (6E10) (1:1000, Cat. 803001, BioLegend), HA-tag (1:2000, Cat. 3724, CST), Flag-tag (1:1000, Cat. F7425, Sigma), Myc-tag (1:2000, Cat. sc-40, Santa Cruz), GST-tag (1:1000, Cat. 2625, CST), AcK (1:1000, Cat. 9441, CST), AcK (1:1000, Cat. 9814, CST), HRP-labelled anti-rabbit (1:5000, Cat. 7074, CST) and anti-mouse (1:5000, Cat. 7076, CST) secondary antibodies

Antibody against GFP (1:1000, Cat. 2956, CST), validated by the producer in their publication:

Oh, K. H. & Kim, H. BK channel clustering is required for normal behavioral alcohol sensitivity in *C. elegans*. *Sci Rep-Uk* 9, doi:ARTN 1022410.1038/s41598-019-46615-9 (2019).

Antibody against Actin (1:2000, Cat. A5441, Sigma), validated by previous colleagues and published:

Sorrentino, V. et al. Enhancing mitochondrial proteostasis reduces amyloid-beta proteotoxicity. *Nature* 552, 187–+, doi:10.1038/nature25143 (2017).

H3K18Ac (1:1000, Cat. 07-354, Merck), validated by the producer in their publication:

Suka, N., Suka, Y., Carmen, A. A., Wu, J. S. & Grunstein, M. Highly specific antibodies determine histone acetylation site usage in yeast heterochromatin and euchromatin. *Mol Cell* 8, 473–479, doi:10.1016/S1097-2765(01)00301-X (2001).

H3K27Ac (1:1000, Cat. ab4729, abcam), validated by the producer in their publication:

Liu, T. et al. Broad chromosomal domains of histone modification patterns in *C. elegans*. *Genome Res* 21, 227–236, doi:10.1101/gr.115519.110 (2011).

H3K9Ac (1:1000, Cat. 06-942, Merck), validated by the producer in their publication:

Wang, G. G. et al. Haematopoietic malignancies caused by dysregulation of a chromatin-binding PHD finger. *Nature* 459, 847–U846, doi:10.1038/nature08036 (2009).

H3K4Ac (1:1000, Cat. ab176799, abcam), validated by the producer in their publication:

Zhang, Y. et al. The ZZ domain of p300 mediates specificity of the adjacent HAT domain for histone H3. *Nat Struct Mol Biol* 25, 841–+, doi:10.1038/s41594-018-0114-9 (2018).

Histone 3 (1:1000, Cat. 9715, CST), validated by the producer in their publication:

Rudra, D. et al. Transcription factor Foxp3 and its protein partners form a complex regulatory network. *Nat Immunol* 13, 1010–1019, doi:10.1038/ni.2402 (2012).

Tubulin (1:2000, Cat. T5168, Sigma), validated by previous colleagues and published:

Sorrentino, V. et al. Enhancing mitochondrial proteostasis reduces amyloid-beta proteotoxicity. *Nature* 552, 187–+, doi:10.1038/nature25143 (2017).

H3K27Me3 (1:1000, Cat. 07-449, millipore), validated by the producer in their publication:

Vandamme, J. et al. The *C. elegans* H3K27 Demethylase UTX-1 Is Essential for Normal Development, Independent of Its Enzymatic Activity. *Plos Genet* 8, doi:ARTN e100264710.1371/journal.pgen.1002647 (2012).

H3K27Me2 (1:1000, Cat. ab24684, abcam), validated by the producer in their publication:

Vandamme, J. et al. The *C. elegans* H3K27 Demethylase UTX-1 Is Essential for Normal Development, Independent of Its Enzymatic Activity. *Plos Genet* 8, doi:ARTN e100264710.1371/journal.pgen.1002647 (2012).

H3K27Me1 (1:1000, Cat. 07-448, millipore), validated by the producer in their publication:

Liu, T. et al. Broad chromosomal domains of histone modification patterns in *C. elegans*. *Genome Res* 21, 227–236, doi:10.1101/gr.115519.110 (2011).

H3K9Me1 (1:1000, Cat. 07-450, millipore), validated by the producer in their publication:

Villeneuve, L. M. et al. Enhanced microRNA-125b Levels in Vascular Smooth Muscle Cells of Diabetic db/db Mice Leads to Increased Inflammatory Gene Expression by Targeting the Histone Methyltransferase Suv39h1. *Arterioscl Throm Vas* 30, E199–E200 (2010).

H3K4Me3 (1:1000, Cat. 07-473, millipore), validated by the producer in their publication:

Wang, G. G. et al. Haematopoietic malignancies caused by dysregulation of a chromatin-binding PHD finger. *Nature* 459, 847–U846, doi:10.1038/nature08036 (2009).

Histone 4 (1:1000, Cat. sc-10810, Santa Cruz), validated by previous colleagues and published:

Matilainen, O., Sleiman, M. S. B., Quiros, P. M., Garcia, S. M. D. A. & Auwerx, J. The chromatin remodeling factor ISW-1 integrates organismal responses against nuclear and mitochondrial stress. *Nat Commun* 8, doi:ARTN 1818

H4K5Ac (1:1000, Cat. ab51997, abcam), validated by previous colleagues and published:

Shimada, M. et al. Gene-Specific H1 Eviction through a Transcriptional Activator -> p300 -> NAP1 -> H1 Pathway. *Mol Cell* 74, 268–+, doi:10.1016/j.molcel.2019.02.016 (2019).

β -amyloid 1–16 (6E10) (1:1000, Cat. 803001, BioLegend), validated by previous colleagues and published:

Sorrentino, V. et al. Enhancing mitochondrial proteostasis reduces amyloid-beta proteotoxicity. *Nature* 552, 187–+, doi:10.1038/nature25143 (2017).

HA-tag (1:2000, Cat. 3724, CST), validated by the producer in their publication:

Tian, Y. et al. Mitochondrial Stress Induces Chromatin Reorganization to Promote Longevity and UPR(mt). *Cell* 165, 1197–1208, doi:10.1016/j.cell.2016.04.011 (2016).

Flag-tag (1:1000, Cat. F7425, Sigma), validated by the producer in their publication:

Lin, S. Y. et al. GSK3-TIP60-ULK1 Signaling Pathway Links Growth Factor Deprivation to Autophagy. *Science* 336, 477–481,

doi:10.1126/science.1217032 (2012).

Myc-tag (1:2000, Cat. sc-40, Santa Cruz), validated by the producer in their publication:

Lin, S. Y. et al. GSK3-TIP60-ULK1 Signaling Pathway Links Growth Factor Deprivation to Autophagy. Science 336, 477-481, doi:10.1126/science.1217032 (2012).

GST-tag (1:1000, Cat. 2625, CST), validated by the producer in their publication:

Wang, B. et al. TRAF2 and OTUD7B govern a ubiquitin-dependent switch that regulates mTORC2 signalling. Nature 545, 365-+, doi:10.1038/nature22344 (2017).

AcK (1:1000, Cat. 9441, CST), validated by the producer in their publication:

Lin, S. Y. et al. GSK3-TIP60-ULK1 Signaling Pathway Links Growth Factor Deprivation to Autophagy. Science 336, 477-481, doi:10.1126/science.1217032 (2012).

AcK (1:1000, Cat. 9814, CST), validated by the producer in their publication:

Xu, M. et al. An acetate switch regulates stress erythropoiesis. Nat Med 20, 1018-1026, doi:10.1038/nm.3587 (2014).

Eukaryotic cell lines

Policy information about [cell lines](#)

Cell line source(s)	The human hepatoma cell line HepG2 was obtained from ATCC. Crebbpfl/fl; Ep300fl/fl mouse embryonic fibroblasts (MEFs) (Kasper, L. H. et al. The EMBO journal, 2010) were provided by Dr. Paul K Brindle (St. Jude Children's Research Hospital, USA)
Authentication	All the cell lines have been authenticated by morphology, karyotyping and PCR-based approaches
Mycoplasma contamination	All cell lines tested negative for mycoplasma contamination
Commonly misidentified lines (See ICLAC register)	No commonly misidentified cell lines were used

Animals and other organisms

Policy information about [studies involving animals](#); [ARRIVE guidelines](#) recommended for reporting animal research

Laboratory animals	The Bristol strain (N2) was used as the wild-type strain. SJ4100 (zcls13[hsp-6p::GFP]), MQ887 (isp-1(qm150)IV), MQ130 (clk-1(qm30)III), QC118 (atfs-1(et18)), OP675 (atfs-1::TY1::EGFP::3xFLAG), GMC101 (dvIs100 [unc-54p::A-beta-1-42::unc-54 3'-UTR + mtl-2p::GFP]) and CL2122 (dvIs15 [(pPD30.38) unc-54(vector) + (pCL26) mtl-2::GFP]) were obtained from the Caenorhabditis Genetics Center (CGC; Minneapolis, MN). Strains with jmjd-3.1 overexpression line #1 AUW3 (N2, epfls3[myo-2p::cfp, jmjd-3.1p::jmjd-3.1]; zcls13[hsp-6p::gfp]V) and line #2 AUW4 (N2, epfls4[myo-2p::cfp, jmjd-3.1p::jmjd-3.1]; zcls13[hsp-6p::gfp]V) were described previously (Merkwirth, C. et al. Cell, 2016). The strain atfs-1(et18); zcls13[hsp-6p::GFP] was generated by crossing the SJ4100 (zcls13[hsp-6p::GFP]) males with the QC118 (atfs-1(et18)) early L4 hermaphrodites. For all experiments involving C. elegans, hermaphrodites were used and worms were harvested at L4/young adult stage, unless otherwise specified in the figure legends.
Wild animals	The study did not involve wild animals
Field-collected samples	The study did not involve samples collected from the field
Ethics oversight	The study did not involve ethics oversight

Note that full information on the approval of the study protocol must also be provided in the manuscript.

ChIP-seq

Data deposition

- Confirm that both raw and final processed data have been deposited in a public database such as [GEO](#).
- Confirm that you have deposited or provided access to graph files (e.g. BED files) for the called peaks.

Data access links <i>May remain private before publication.</i>	The raw sequenced data generated in this study were deposited in the NCBI Gene Expression Omnibus (GEO) database (https://www.ncbi.nlm.nih.gov/geo/) under accession number GSE148328
Files in database submission	H3K18Ac_ev.fq.gz; H3K27Ac_ev.fq.gz; H3K18Ac_cco-1.fq.gz; H3K27Ac_cco-1.fq.gz; Processed ChIP-seq data_Worm_TYL
Genome browser session (e.g. UCSC)	No longer applicable

Methodology

Replicates	There is one ChIP-seq experimental replicate for each of the four conditions: H3K18Ac_ev, H3K27Ac_ev, H3K18Ac_cco-1 and H3K27Ac_cco-1. Note that both H3K18Ac and H3K27Ac are active transcription marks and show similar peak patterns
------------	---

Sequencing depth	<p>The sequence depth of each sample is as follows: H3K18Ac_ev.fq.gz, total reads: 24,133,078, mapped reads: 17,848,286; H3K27Ac_ev.fq.gz, total reads: 24,252,596, mapped reads: 19,626,058; H3K18Ac_cco-1.fq.gz, total reads: 24,014,423, mapped reads: 18,038,979; H3K27Ac_cco-1.fq.gz, total reads: 25,032,450, mapped reads: 205,556,77. The sequencing performed for all samples is single-end 50 bp sequencing</p>
Antibodies	<p>Antibodies against H3K18Ac (1:100, Cat. 07-354, Merck) or H3K27Ac (1:100, Cat. ab4729, abcam) were used for ChIP</p>
Peak calling parameters	<p>All reads were aligned to the reference worm genome (WBcel235 ce11 top-level and Ensembl release 89 annotation) using the Bowtie 2 aligner (version 2.3.5) with the following parameters (output was then processed using samtools package before saving the bam file): bowtie2 -p 16 -x \$index -U \$read samtools view -@ 16 -Sb -q 10 samtools sort -@ 16 > \${SAMPLE}.bam Output Bam files were then indexed using `samtools index` tool with default parameters. For peak calling, we used the macs2 software (version 2.1.2) with the following parameters: macs2 callpeak -t \${SAMPLE_1}.bam -c \${SAMPLE_2}.bam -f BAM -g ce --outdir \$OUT -n \$SAMPLE --broad 2; intersectBed of the BEDTools (version 2.26.0) package was used to generate the intersects and read counting</p>
Data quality	<p>Raw sequencing data quality was checked with the FastQC (version 0.11.7) software. Quality of alignment and peaks were assessed using the ChIPQC (version 1.18.2) R package before proceeding with the analysis. Reported peaks were filtered out based on the associated FDR value (default value of FDR 0.05)</p>
Software	<p>FastQC (version 0.11.7) was used to verify the quality of the raw sequencing reads. bowtie2 (version 2.3.5) was used to align reads to genome. SAMtools (version 1.4.1) package was used to filter and process the sam and bam files (view, sort and index functions). MACS2 (version 2.1.2) (callpeak function) was used to callpeaks between the compared conditions. ChIPQC (version 1.18.2) was used to assess the quality of the alignments and peaks obtained. BEDTools (version 2.26.0) (intersectBed and bamToBed functions) was used to generate the intersects and read counting</p>